Formation of Amphibole-Bearing Peridotite and Amphibole-Bearing Pyroxenite through Hydrous Melt-Peridotite Reaction and In Situ Crystallization: An Experimental Study

Chunguang Wang[1], Yan Liang[2], and Wenliang Xu[1]

[1]Jilin University
[2]Brown University

November 22, 2022

Abstract

Amphibole is a common hydrous mineral in mantle rocks. To better understand the processes leading to the formation of amphibole-bearing peridotites and pyroxenites in mantle rocks, we have undertaken an experimental study reacting lherzolite with hydrous basaltic melts in Au-Pd capsules using the reaction couple method. Two melts were examined, a basaltic andesite and a basalt, each containing 4 wt% of water. The experiments were run at 1200°C and 1 GPa for 3 or 12 h, and then cooled to 880°C and 0.8 GPa over 49 h. The reaction at 1200°C and 1 GPa produced a melt-bearing orthopyroxenite-dunite sequence. The cooling stimulates crystallization of orthopyroxene, clinopyroxene, amphibole, and plagioclase, leading to the formation of an amphibole-bearing gabbronorite–orthopyroxenite–peridotite sequence. Compositional variations of minerals in the experiments are controlled by temperature, pressure, and reacting melt composition. Texture, mineralogy, and mineral compositional variation trends obtained from the experiments are similar to those from mantle xenoliths and peridotite massif from the field including amphibole-bearing peridotites and amphibole-bearing pyroxenite and amphibolite that are spatially associated with peridotites, underscoring the importance of hydrous melt-peridotite reaction in the formation of these amphibole-bearing rocks in the upper mantle. Amphiboles in some field samples have distinct textual and mineralogical features and their compositional variation trends are different from that defined by the melt-peridotite reaction experiments. These amphiboles are either crystallized from the host magma that entrained the xenoliths or product of hydrothermal alterations at shallow depths.

Posted on 22 Nov 2022 — CC-BY 4.0 — https://doi.org/10.1002/essoar.10501571.1 — This a preprint and has not been peer reviewed. Data may be preliminary.

Formation of Amphibole-Bearing Peridotite and Amphibole-Bearing Pyroxenite through Hydrous Melt-Peridotite Reaction and In Situ Crystallization: An Experimental Study

Chunguang Wang[1, 2, *], Yan Liang[2], and Wenliang Xu[1]

[1] College of Earth Sciences, Jilin University, Changchun 130061, China

[2] Department of Earth, Environmental and Planetary Sciences, Brown University, Providence, RI 02912, USA

Corresponding author: Chunguang Wang (c_wang@jlu.edu.cn)

Key Points:

- Consequence of hydrous melt-peridotite reaction followed by in-situ crystallization was investigated experimentally.
- Hydrous melt-lherzolite reactive crystallization forms amphibole-bearing peridotite and amphibole-bearing pyroxenite.
- Chemical composition of amphibole can be used to identify hydrous melt and peridotite interaction in the upper mantle.

Abstract

Amphibole is a common hydrous mineral in mantle rocks. To better understand the processes leading to the formation of amphibole-bearing peridotites and pyroxenites in mantle rocks, we have undertaken an experimental study reacting lherzolite with hydrous basaltic melts in Au-Pd capsules using the reaction couple method. Two melts were examined, a basaltic andesite and a basalt, each containing 4 wt% of water. The experiments were run at 1200°C and 1 GPa for 3 or 12 h, and then cooled to 880°C and 0.8 GPa over 49 h. The reaction at 1200°C and 1 GPa produced a melt-bearing orthopyroxenite-dunite sequence. The cooling stimulates crystallization of orthopyroxene, clinopyroxene, amphibole, and plagioclase, leading to the formation of an amphibole-bearing gabbronorite–orthopyroxenite–peridotite sequence. Compositional variations of minerals in the experiments are controlled by temperature, pressure, and reacting melt composition. Texture, mineralogy, and mineral compositional variation trends obtained from the experiments are similar to those from mantle xenoliths and peridotite massif from the field including amphibole-bearing peridotites and amphibole-bearing pyroxenite and amphibolite that are spatially associated with peridotites, underscoring the importance of hydrous melt-peridotite reaction in the formation of these amphibole-bearing rocks in the upper mantle. Amphiboles in some field samples have distinct textual and mineralogical features and their compositional variation trends are different from that defined by the melt-peridotite reaction experiments. These amphiboles are either crystallized from the host magma that entrained the xenoliths or product of hydrothermal alterations at shallow depths.

1. Introduction

Amphibole is commonly observed in mantle xenoliths (e.g., Wilshier and Schwarzman, 1971; Dautria et al., 1987; Moine et al., 2001; Xu et al., 2010) and massif peridotites (e.g., Agrinier et al., 1993; Zanetti et al., 1996; Ohara and Ishii, 1998; Li et al., 2018) from a range of geological settings, such as arcs (e.g., Ohara and Ishii, 1998; Ishimaru et al., 2007; Bénard and Ionov, 2013), ocean islands (e.g., Clague and Bohrson, 1991; Moine et al., 2001), continental margins (Francis, 1976a, 1976b; Agrinier et al., 1993), and intracontinental regions (e.g., Wilshier and Schwarzman, 1971; Dautria et al., 1987; O'Reilly et al., 1991; Xu et al., 2010). Typical lithologies include amphibole-bearing peridotite, amphibole-bearing pyroxenite, and amphibolite. In general, amphibole occurs either interstitial to anhydrous minerals in peridotites or in amphibole-rich veins or bodies in peridotites.

Based on field studies, a number of mechanisms have been proposed for the formation of amphibole in mantle xenoliths and massif peridotites. Frey and Prinz (1978) reported a set of amphibole-bearing peridotite and pyroxenite xenoliths in basanites from Grand Canyon and San Carlos, Arizona, USA. They suggested that the poikilitic amphiboles enclosing olivines and spinels were accumulations of basaltic magma. Agrinier et al. (1993) described different types of amphibole in a peridotite massif from Zabargad Island, Red Sea. Amphiboles that exist as individual grains interstitial between olivines and spinels were inferred to be products of reaction between the peridotites and hydrous fluids, and amphiboles that occur in shear zones and mylonitic bands to be results of seawater alteration after emplacement of the massif. Coltorti et al. (2004) and Bonadiman et al. (2014) inferred that the disseminated amphiboles and vein amphiboles in peridotite entrained by basalts from Victoria Land, Antarctica were formed by reaction between clinopyroxene and a batch of metasomatic melt. The different occurrences are due to different melt-to-rock ratios. The chief objective of the present study is to develop a set of

criteria that can be used to distinguish amphiboles formed by hydrous melt and peridotite reaction from those produced by fluid-peridotite interaction or hydrothermal alteration.

The processes and consequences of melt-peridotite interaction have been extensively studied through laboratory dissolution experiments for a range of starting compositions and P-T conditions in anhydrous systems (e.g., Daines and Kohlstedt, 1994; Yaxley and Green, 1998; Takahashi and Nakajima, 2002; Morgan and Liang, 2003, 2005; Beck et al., 2006; Lambart et al., 2009, 2012; Van den Bleeken et al., 2010, 2011; Wang et al., 2013). However, comparable studies in hydrous systems are limited (Sekine and Wyllie, 1983; Carroll and Wyllie, 1989; Johnston and Wyllie, 1990; Kelemen et al., 1990; Sen and Dunn, 1994; Rapp et al., 1999; Mallik et al., 2015; Mandler and Grove, 2016; Wang et al., 2016). Sen and Dunn (1994) conducted reaction experiments by packing a powdered spinel lherzolite layer against a powdered amphibolite (1.5 wt% water) layer in graphite-lined Pt capsules at 1.5-2.0 GPa and 950-1025°C. They observed amphiboles along the boundaries of olivine, pyroxenes, and spinel. The amphiboles have compositions similar to those in amphibole-bearing peridotite from the field. They inferred that reaction of olivine, primary orthopyroxene, clinopyroxene, and spinel with hydrous melt forms amphibole and Fe-rich orthopyroxene and that a further reaction would form amphibole-bearing harzburgite (free of clinopyroxene and spinel) and finally amphibole-bearing orthopyroxenite (free of clinopyroxene, spinel, and olivine). In a recent melt-peridotite reaction study (Wang et al., 2016), we reacted a layer of lherzolite with a layer of water-added (4 wt%) basaltic andesite in a Au-Pd lined graphite capsule at 1200°C and 1 GPa (run BAH8 in Wang et al., 2016). Figure 1a is a back-scattered electron (BSE) image showing the orthopyroxenite-dunite sequence formed in the peridotite half of the reaction couple and quenched amphibole crystals in the interstitial melts around the orthopyroxenite-dunite boundary. The presence of quenched amphiboles in this isothermal hydrous melt-peridotite reaction experiment is intriguing. The reacting melt around the orthopyroxenite must be near amphibole saturation at 1200°C and 1 GPa.

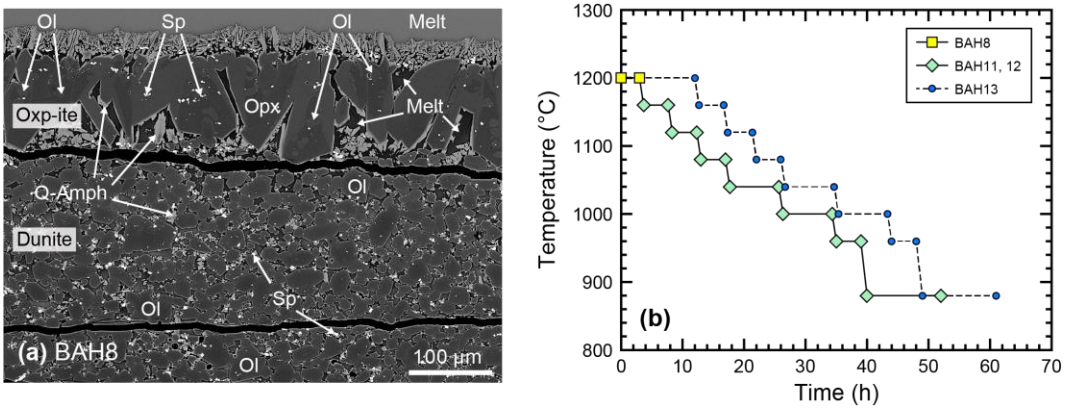

Figure 1. (a) Back-scattered electron (BSE) image that recalls the result (interface region) of hydrous basaltic andesite and peridotite reaction experiments conducted at 1200 °C and 1 GPa (BAH8, Wang et al., 2016) using the same capsule setup as those in the present study. Ol = olivine; Opx = orthopyroxene; Sp = spinel; Q-Amph = quench amphibole; Opx-ite = orthopyroxenite. (b) Temperature histories of the melt-rock reaction experiments. Zero time marks the beginning of the experiment, when the target temperature of 1200°C was reached. Experiments BAH11 and MBH12 were run using the same temperature-pressure path. BAH13 was hold at 1200°C for a longer duration (12 h) than BAH11 and MBH12 (3 h). Temperature and duration used in the isothermal experiment BAH8 (1200°C, 3 h, without step cooling, Wang et al., 2016) is also shown for comparison.

In this study, we further expand the isothermal hydrous melt-peridotite reaction experiments of Wang et al. (2016) by considering two hydrous melts (basalt and basaltic andesite) and by allowing in situ crystallization of reacting melts through step cooling of experimental charges (to 880°C and 0.8 GPa) at the end of isothermal reaction at 1200°C and 1 GPa (Fig. 1b). The quenched experimental charge enables us to examine the texture, mineralogy, and mineral compositional variation formed after the hydrous melt and peridotite reaction. Results from these experiments allow us to better understand the processes leading to the formation of amphibole-bearing peridotites and pyroxenites.

The remaining part of this paper is organized as follows. In the next section, we describe the starting materials and experimental methods. We present the textural and chemical features of the run products, compare the results with those observed in previous experimental studies, and discuss the processes leading to the formation of amphibole-bearing peridotites and pyroxenites. We then compare texture and mineral compositions observed in the experiments with those from amphibole-bearing peridotites and pyroxenites in mantle xenoliths and massif peridotites. We show that water and melt-peridotite reaction are important in determining the lithology and mineral compositional variation in the mantle rocks.

Table 1 Starting compositions

Oxide (wt%)	Basaltic andesite MONT147	MORB D44A	Spinel lherzolite WFY-2[b]			
			Olivine	Opx	Cpx	Spinel
SiO_2	54.86	50.13	40.25	54.39	51.45	0.08
TiO_2	0.77	1.25	0.01	0.09	0.39	0.15
Al_2O_3	18.78	16.31	0.04	4.44	5.49	54.26
Cr_2O_3			0.03	0.39	0.81	12.83
FeO[a]	8.96	8.85	9.82	6.25	2.93	10.87
MnO	0.21	0.17	0.12	0.12	0.11	0.15
MgO	3.66	8.72	48.41	32.46	16.27	20.50
CaO	8.80	12.50	0.09	0.88	20.55	0.01
Na_2O	3.08	2.63	0.00	0.12	0.98	0.02
K_2O	0.78	0.02	0.00	0.01	0.00	0.01
NiO			0.38	0.11	0.04	0.35
P_2O_5	0.14	0.08				
Total	100.04	100.66	99.15	99.26	99.02	99.23
Mg#	42.13	63.72	89.78	90.25	90.82	77.07
Cr#						13.69

Mg# = 100 × Mg/(Mg + Fe), atomic ratio; Cr# = 100 × Cr/(Cr + Al), atomic ratio; Opx = orthopyroxene; Cpx = clinopyroxene.
[a] Total Fe as FeO
[b] WFY-2 consists of 60 % olivine, 23 % opx, 12 % cpx, and 5 % spinel

2. Methods

Hydrous melt-peridotite reaction and in situ crystallization experiments were conducted using the reaction couple method and a 19.1-mm piston-cylinder apparatus at Brown University.

Reaction couples were made by juxtaposing a powdered starting basalt layer against a powdered spinel lherzolite layer at a length ratio of ~5:3 in Au-Pd lined graphite capsules. Each experiment consists of four stages: pressurization to 1 GPa at room temperature, a dwell at 1200°C and 1 GPa, a subsequent step cooling to 880°C and 0.8 GPa, and a final dwell at 880°C and 0.8 GPa. The starting melt and mineral compositions are listed in Table 1. Run conditions for each experiment are listed in Table 2, and the temperature-time paths are shown in Fig. 1b.

2.1. Starting compositions

The starting lherzolite (sample WFY-2) was obtained by mixing optically clean olivine (60%), orthopyroxene (23%), clinopyroxene (12%), and spinel (5%) from a disaggregated fertile spinel lherzolite xenolith entrained by alkali basalt from Huinan, China. The starting materials for the reacting melts are a basaltic andesite (sample Mont147) from Montserrat and a mid-ocean ridge basalt (MORB, sample D44A) from Southern East Pacific Rise to which we added 4 wt% water during sample loading. The starting lherzolite and basaltic andesite were used in isothermal hydrous melt-rock reaction experiments of Wang et al. (2016), and the MORB was used in anhydrous reaction and crystallization experiments of Tursack and Liang (2012) and Saper and Liang (2014). Results from these earlier laboratory studies serve as references or benchmarks for the hydrous reaction and crystallization experiments reported in this study. The starting samples were ground separately in ethanol using an agate mortar and pestle for 2-4 h and stored at 110°C before use.

2.2. Experimental procedures

The furnace assembly consists of a Au-Pd lined graphite capsule in a MgO sleeve sandwiched between two crushable MgO spacers in Pyrex tubing, NaCl sleeve, and straight-walled graphite heater. The cylindrical graphite capsule (6.5 mm OD, 7 mm long) was lined with a Au_{75}-Pd_{25} inner capsule (3 mm OD, 2.8 mm ID, 5 mm long). To make a reaction couple, we first packed the peridotite powder in the lower part of the Au-Pd capsule and filled the remaining part of the capsule with the basaltic andesite or MORB powder. We then added deionized water using a micro syringe and sealed the Au-Pd capsule using a micro arc welder immediately after water loading. We weighed the capsule before and after each loading to ensure that the water-to-basalt weight ratio is around 4:96 (i.e., 4 wt% water). The arc welder has a thin tungsten electrode (0.6 mm in diameter) and operates under a stream of protective argon gas. It allows pinpoint welding with a very small heat affected area. The weight loss due to the welding is less than 0.5% (evaporation of water and Au-Pd alloy). Finally, we loaded the sealed Au-Pd capsule in the graphite capsule and capped the graphite capsule with a 0.5 mm thick graphite lid. The furnace assembly and capsule used in this study are the same as those used in experiments BAH8 and BADH15 in Wang et al. (2016). Oxygen fugacity of the experiments is maintained at -8 to -9 logarithmic unit, estimated using the method of Barr and Grove (2010).

To conduct a reaction experiment, the charge was cold pressurized to 1 GPa, followed by heating to 1200°C at 75°C/min while maintaining pressure. The run was held at 1200°C and 1 GPa for 3 h for runs BAH11 and MBH12 and 12 h for BAH13. The run was then cooled to 880°C over 7 steps in 49 h (Fig. 1b). Each step cooling was performed at a rate of 1°C/min, followed by a 4 or 8 h dwell at the specific temperature. The pressure, which was not adjusted during cooling, gradually decreased to 0.8 GPa at the final dwell (880°C). At the end of experiment, the charge was quenched by cutting the power supply while maintaining the

157 pressure. The heating and step cooling were operated through a Eurotherm controller, and
158 temperature was measured using a $W_{97}Re_3$-$W_{75}Re_{25}$ thermocouple with an uncertainty of 10°C
159 (Morgan and Liang, 2005). No friction correction was applied to the pressure. The retrieved
160 experimental charge was checked under a binocular microscope to ensure no crack in the Au-Pd
161 capsule. The capsule was then mounted in epoxy and polished gradually using a 600-mesh SiC
162 polishing paper in water until the cylindrical axis was exposed. During polish, the Au-Pd capsule
163 was checked using a microscope under reflecting light to ensure no leak exist; the exposed
164 surface was soaked in epoxy and stored in a vacuum chamber for several times, so that cracks
165 formed during quench were puttied. The exposed surface was finally polished to 1 μm finish for
166 electron microprobe analysis.

167 ### 2.3. Microprobe analysis

168 Collection of back-scattered electron images and X-ray concentration maps and
169 measurements of mineral compositions were carried out using a Cameca SX-100 electron
170 microprobe at Brown University. An accelerating voltage of 20 kV and a beam current of 25 nA
171 were used to collect X-ray concentration maps. A 10 μm diameter beam was used for glass
172 analyses and a focused beam for mineral analyses. Accelerating voltage and beam current were
173 15 kV and 10 nA for glass analyses, 20 kV and 15 nA for plagioclase analyses, and 20 kV and 25
174 nA for olivine, pyroxene, amphibole, and spinel analyses, respectively. Sodium was analyzed
175 first with counting times of 10 s for peak and 5 s for background to minimize volatilization.
176 Counting times for other elements were 20-30 s for peak, and 10-15 s for background on each
177 side of the peak. Natural standards were used for calibration.

Table 2 Summary of experimental conditions

Run#	BAH8[a]	BAH11	BAH13	MBH12
Starting melt	Basaltic andesite	Basaltic andesite	Basaltic andesite	MORB
Pressure (GPa)	1	1 (0.8)[b]	1 (0.8)[a]	1 (0.8)[a]
Initial temp (°C)	1200 (3 h)[c]	1200 (3 h)[c]	1200 (12 h)[c]	1200 (3 h)[c]
Final temp (°C)		880 (12 h)[c]	880 (12 h)[c]	880 (12 h)[c]
Cooling process	Quench	Step cooling[d]	Step cooling[d]	Step cooling[d]
Total duration (h)	3	52	61	52
RBL lithologies	Glass	Amph gabbronorite	Amph gabbronorite	Amph gabbronorite
	Opx-ite	Amph-bearing opx-ite	Amph-bearing opx-ite	Amph-bearing opx-ite
	Dunite	Amph-bearing harz	Amph-bearing harz	Amph-bearing lherz

RBL = reactive boundary layer; Amph = amphibole; Opx-ite = orthopyroxenite; Harz = harzburgite; Lherz = lherzolite.
[a] Isobaric and isothermal experiment from Wang et al. (2016)
[b] Number in parenthesis is the pressure at final temperature
[c] Number in parenthesis is the duration at the initial or final temperature
[d] Step cooling is at a rate of 1°C/min to specific temperatures maintained for 4 or 8 h

178 ## 3. Results and discussion

179 Three hydrous melt-peridotite reaction and crystallization experiments were conducted
180 using the two starting melts. They were built on melt-peridotite reaction experiments using
181 similar setups and starting compositions that are either hydrous but isothermal (Wang et al.,
182 2016) or step-cooling but anhydrous (Tursack and Liang, 2012; Saper and Liang, 2014).

Experiments BAH11 and BAH13 use the 4 wt% water-added basaltic andesite as the starting melt, and experiment MBH12 uses the 4 wt% water-added MORB as the starting melt. We did not measure water contents in the experimental glasses because of the crystalline nature of the experimental charges. Judging from the presence of amphibole and vesicles in the experiments and integrity of the Au-Pd capsules (Fig. 2 and supporting Figure S1), we conclude that these capsules retained a significant fraction of water in the system and our reacting melts were indeed hydrous at run conditions. Mineralogical and textural features of the experiments are summarized in Table 2. Representative BSE images of the run products are displayed in Figs. 2 and 3. Mineral compositions that were obtained from spot microprobe analyses are presented in Figs. 4-10, and 12. Additional BSE images and mineral composition profiles (Figures S1-S8) can be found in the Supporting Information, and electron microprobe data are archived at Mendeley Data (http://dx.doi.org/10.17632/895f6y8chd.1).

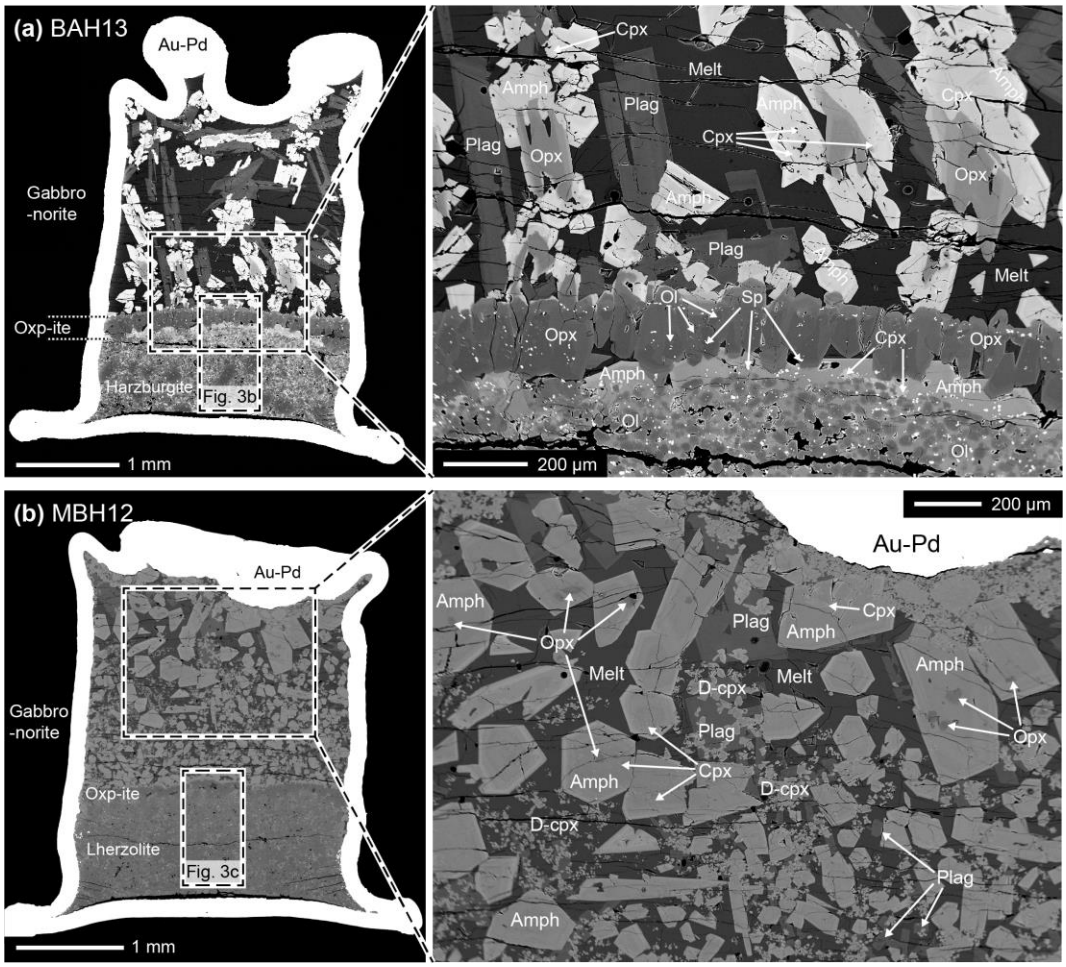

Figure 2. Back-scattered electron (BSE) images showing the results of the reactive crystallization experiments. (a) BAH13 (hydrous basaltic andesite vs. lherzolite, 12 h reaction). (b) MBH12 (hydrous MORB vs. lherzolite, 3 h reaction). The left panels are the entire experimental charges, and the right panels are the views of the gabbronorite regions. Ol = olivine; Opx = orthopyroxene; Cpx = clinopyroxene; D-cpx = disseminated clinopyroxene; Sp = spinel; Amph = amphibole; Plag = plagioclase; Opx-ite = orthopyroxenite.

3.1. Lithologies and textures

After reaction at 1200°C and 1 GPa and step cooling to 880°C and 0.8 GPa, each experimental charge consists of three distinct lithological zones: an amphibole gabbronorite, an amphibole-bearing peridotite, and an amphibole-bearing orthopyroxenite (100-300 μm thick) that separates the former two lithological zones (Fig. 2 and Figure S1). The amphibole gabbronorite, which is absent in the isothermal experiments of Tursack and Liang (2012) and Wang et al. (2016), consists of orthopyroxene, clinopyroxene, amphibole, plagioclase, and quenched melt (Fig. 2). Orthopyroxenes are subhedral and often surrounded by large euhedral amphiboles or present as inclusions around the central part of amphiboles (Fig. 2 and Figure S1). Clinopyroxene grains are anhedral and small. They are generally enclosed around rim parts of the large amphiboles, and some clinopyroxenes in gabbronorite from MBH12 are dispersed in melt or enclosed in plagioclases (Fig. 3b). Plagioclases are tabular-shaped with modal abundance decrease from Runs BAH11 and BAH13 to Run MBH12. Ulvöspinel is observed in the gabbronorite section in experiment BAH11 (Figure S1), a byproduct of reactive crystallization at the reducing condition.

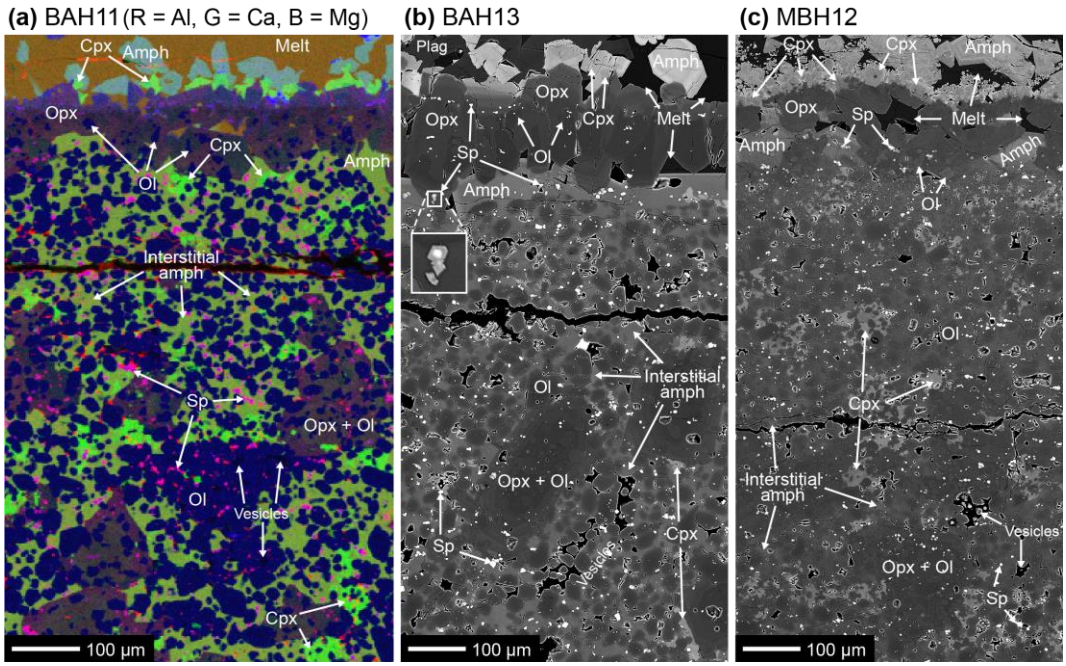

Figure 3. False-colored composite X-ray concentration map (a) and back-scattered electron (BSE) images (b and c) showing the amphibole-bearing orthopyroxenite and peridotite regions of experimental charges. (a) BAH11 (hydrous basaltic andesite vs. lherzolite, 3 h reaction). (b) BAH13 (hydrous basaltic andesite vs. lherzolite, 12 h reaction). (c) MBH12 (hydrous MORB vs. lherzolite, 3 h reaction). Ol = olivine; Opx = orthopyroxene; Cpx = clinopyroxene; Sp = spinel, Amph = amphibole; Plag = plagioclase.

The amphibole-bearing peridotite consists of olivine, orthopyroxene, clinopyroxene, spinel, and amphibole (Fig. 3). Olivines are round in shape and small in size (<60 μm in diameter). Orthopyroxenes are large (up to 350 μm in length) and core-to-rim zoned in the X-ray concentration map and BSE images (Fig. 3). The orthopyroxenes enclose small rounded olivines and spinels forming a poikilitic texture. Clinopyroxenes are embayed in shape and low in modal abundance (<7 vol%). Clinopyroxene is more abundant in the peridotite when the reacting melt is the hydrous MORB (run MBH12) than those when the reacting melt is the hydrous basaltic

andesite (BAH11 and BAH13, cf. Fig. 3c to Figs. 3a and 3b). Some spinels exhibit euhedral darker rims in the BSE images (insert in Fig. 3b). Amphibole is crystallized interstitial to other minerals throughout the peridotite. Empty vesicles are present where small olivine grains are abundant, but absent in the poikilitic orthopyroxenes. Plagioclase and interstitial melt are not observed in the peridotite region.

The amphibole-bearing orthopyroxenite layer between the amphibole gabbronorite and peridotite is mainly composed of large euhedral orthopyroxenes (up to 200 μm in length) (Fig. 3). These orthopyroxene grains contain small olivine and spinel inclusions (Fig. 3), similar to those formed in the isothermal hydrous reaction experiment BAH8 from Wang et al. (2016). Clinopyroxene and amphibole are observed around the gabbronorite-orthopyroxenite boundary, whereas interstitial melt is observed around the orthopyroxenite-peridotite interface. Interestingly, on the gabbronorite side of the orthopyroxenite in MBH12, orthopyroxenes are partially dissolved and replaced by a layer of clinopyroxene (Fig. 3c), suggesting a reaction relationship between the two minerals.

3.2. Variations in mineral composition

Compositional variations in minerals from the hydrous melt-peridotite reaction experiments are observed both within grain and across lithological regions. Grain-scale variation exists in orthopyroxene, amphibole, plagioclase, and spinel. Cores of large orthopyroxene and amphibole grains have higher Mg# [Mg# = 100 × Mg/(Mg + Fe), in molar] than the rims (Figures S2 and S3). Plagioclase displays oscillatory zoning with an overall decreasing in An# [An# = 100 × Ca/(Ca + Na), in molar] and Al_2O_3 content from core to rim (Figure S4). Spinel grains exhibit core-to-rim zoning in the BSE images (insert in Fig. 2b). The darker rims likely have lower Cr# [Cr# = 100 × Cr/(Cr + Al), in molar] and higher Mg# than the lighter cores. These core-to-rim variations are consistent with crystallization trends.

Figures 4 and 5 display compositional variations of orthopyroxene and amphibole across the gabbronorite, orthopyroxenite, and peridotite sequence. (Compositional profiles for other minerals can be found in Figures S5-S8.) Zero distance marks the approximate position of the gabbronorite-orthopyroxenite interface at the end of the run. This interface is also the boundary separating the crystalline region (melt-bearing orthopyroxenite and dunite) and the crystal-free reacting melt during the reaction at 1200°C (Fig. 1a). Mineral compositions are distinct across the interface for both orthopyroxene and amphibole, although the trends are somewhat obscured by core-to-rim variations. The differences are more pronounced in run BAH11 (basaltic andesite as reacting melt, 3 h reaction at 1200°C, cyan symbols) than the other two runs (blue and red symbols). For longer reaction time (BAH13) and more primitive reacting melt composition (MBH12), compositions of amphiboles and orthopyroxenes in gabbronorite become more similar to those in the peridotite. SiO_2 content in amphibole and Mg# in orthopyroxene and amphibole from the gabbronorite layer are lower than those from the peridotite and orthopyroxenite layers, whereas TiO_2 and MnO contents are higher in the gabbronorite. Na_2O abundance decreases in orthopyroxenes (Fig. 4g) and increases in amphibole (Fig. 5h) from peridotite to gabbronorite. Orthopyroxene and amphibole compositions from each experiment exhibit large variabilities at the same distance in the compositional profiles, consistent with the core-to-rim compositional variations (Figs. 4 and 5).

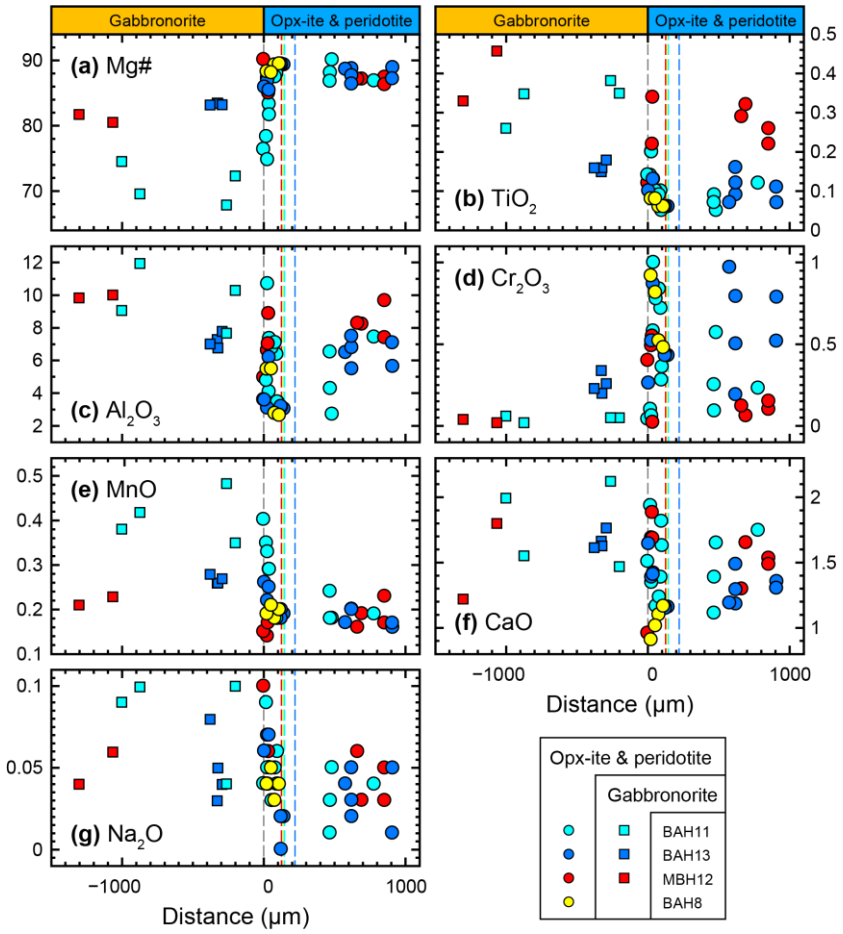

Figure 4. Plots of Mg# and oxide abundances (in wt%) in orthopyroxene as a function of distance from the gabbronorite-orthopyroxenite interface. Circles represent orthopyroxene in the amphibole-bearing orthopyroxenite (opx-ite) and peridotite regions, and squares represent those in the amphibole gabbronorite region of each experiment. Also shown are compositions of orthopyroxene in orthopyroxenite from the isothermal reaction experiment BAH8 from Wang et al. (2016). The dashed gray lines mark the position of gabbronorite-orthopyroxenite interface, and the dashed cyan, blue, red, and yellow lines mark the positions of orthopyroxenite-peridotite interfaces in BAH11, BAH13, BAH12, and BAH8, respectively.

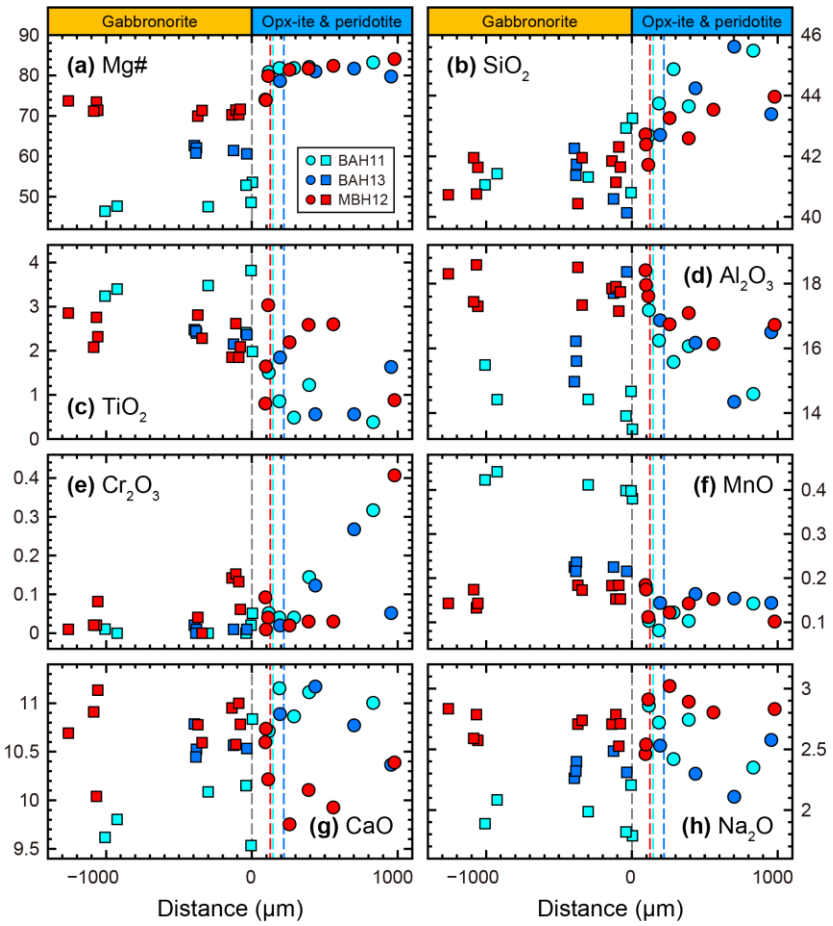

Figure 5. Plots of Mg# and oxide abundances (in wt%) in amphibole as a function of distance from the gabbronorite-orthopyroxenite interface. Circles represent amphibole in the amphibole-bearing orthopyroxenite (opx-ite) and peridotite regions, and squares represent those in the amphibole gabbronorite region of each experiment. The dashed gray lines mark the position of gabbronorite-orthopyroxenite interface, and the dashed cyan, blue, and red lines mark the positions of orthopyroxenite-peridotite interfaces in BAH11, BAH13, and BAH12, respectively.

3.3. Comparison with previous melt-rock reaction experiments

The lithological sequence and mineral compositions of the hydrous melt-peridotite reaction experiments are significantly different from those of the anhydrous cases that have nearly identical starting melt and peridotite compositions. The most remarkable difference between the hydrous reactive crystallization experiments presented here and the anhydrous ones reported by Tursack and Liang (2012) and Saper and Liang (2014) is the formation of amphibole-bearing orthopyroxenite and amphibole-bearing peridotite in the hydrous experiments (Figs. 2 and 3). The two anhydrous reactive crystallization studies (reaction at 1 GPa and 1300-1320°C, followed by a step cooling to 1200°C or 1050°C) used the same starting basalt (sample D44A) as the hydrous run MBH12 but without addition of water. These experiments produced a gabbronorite–wehrlite or a gabbronorite–wehrlite–peridotite sequence. Plagioclase is observed in the wehrlite and peridotite in experiments where the starting lherzolite was mixed with 12% basalt (Saper and Liang, 2014). Plagioclase is not observed in the peridotite layer in the present study.

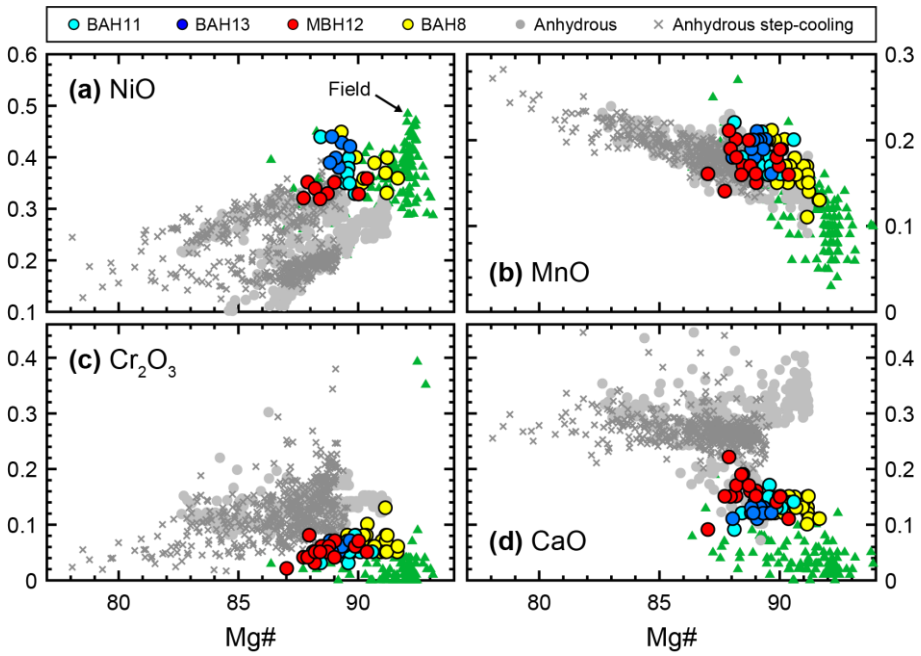

Figure 6. Variations of oxide abundances (in wt%) vs. Mg# in olivine from melt-peridotite reaction experiments and those from field observations of amphibole-bearing mantle rocks (green triangles). Color circles are olivines from the hydrous melt-peridotite reaction experiments BAH11, BAH13, and BAH12 from this study and BAH8 from Wang et al. (2016). Gray circles are olivines from anhydrous isothermal melt-peridotite reaction experiments (Harzdis24 from Morgan and Liang, 2003; Lherzdis4 and Lherzdis5 from Morgan and Liang, 2005; PDET1 from Tursack and Liang, 2012), and gray crosses are those from anhydrous reactive crystallization experiments (PDET1b, PDET1c, and PDET2b from Turack and Liang, 2012; PDLS6 and PDSL11 from Saper and Liang, 2014), all conducted in the same laboratory using similar experimental design and starting compositions. The Mantle xenoliths are from the North China Craton (Xu and Bodinier, 2004; Xu et al., 2010), western US (Wilshier and Schwarzman, 1971; Francis, 1976a, 1976b; Wilshier et al., 1980), Hawaii (Clagu and Bohrson, 1991), Antarctica (Coltorti et al., 2004; Bonadiman et al., 2014), southeastern Australia (O'Reilly et al., 1991; Powell et al., 2004), Kerguelen Islands (Moine et al., 2001), Rhenish Uplands (Witt and Seck, 1989; Witt-Eickschen et al. 2003), Avacha (Bénard and Ionov, 2013), and Ahaggar (Dautria et al., 1987). The massif peridotites are from Lherz (Zanetti et al., 1996), Mariana Trench (Ohara and Ishii, 1998), Zabargad Island (Agrinier, 1993), and Sulu Orogen (Li et al., 2018).

Figures 6-10 compare mineral compositions obtained from the hydrous melt-peridotite reaction experiments with those from the anhydrous ones (for olivine, pyroxenes, spinel, and plagioclase) and phase equilibrium experiments (for amphibole and plagioclase). In general, NiO is positively and MnO is negatively correlated with Mg# in olivine from the melt-rock reaction experiments (Figs. 6a and 6b). Olivine composition from the hydrous melt-rock reaction experiments covers a considerably narrower range than both the isothermal and the step-cooling experiments conducted under anhydrous conditions (Fig. 6). They cluster at the high-Mg# and high-NiO end in the NiO vs. Mg# diagram (Fig. 6a). Olivines from the hydrous experiments have lower CaO and Cr_2O_3 contents and slightly higher MnO content than those from the anhydrous ones (Figs. 6b-6d). Among the hydrous reaction experiments, olivine from the step-cooling ones (cyan, blue, and red circles in Fig. 6) have slightly lower Mg# than the hydrous isothermal one BAH8 (yellow circles in Fig. 6).

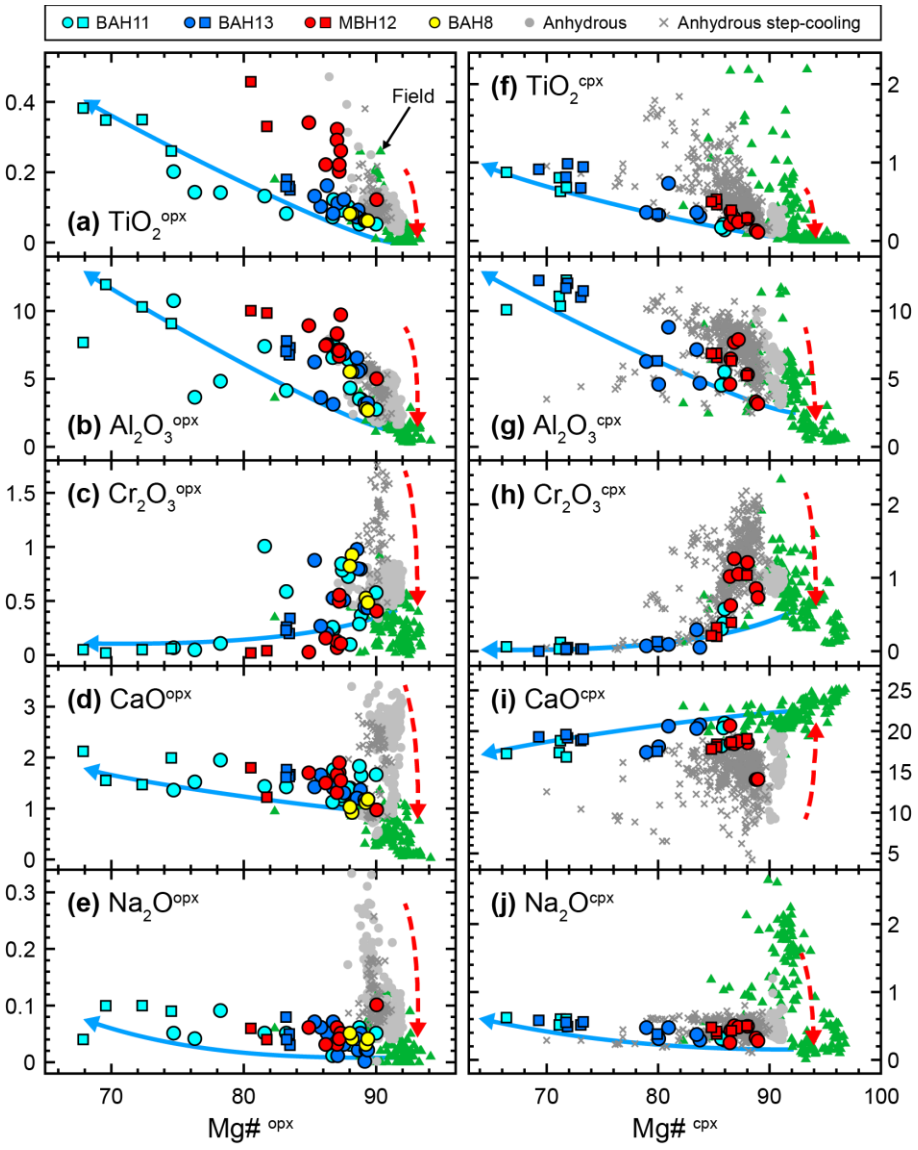

Figure 7. Variations of oxide abundances (in wt%) vs. Mg# in orthopyroxene (a-e) and clinopyroxene (f-j) from melt-peridotite reaction experiments and those from field observations of amphibole-bearing mantle rocks (green triangles). Circles are orthopyroxene in the amphibole-bearing orthopyroxenite and peridotite regions, and squares are those in the amphibole gabbronorite regions in experiments from this study. Source of the experimental and field data are the same as in Fig. 6. The dashed red arrows mark the melting and re-equilibration trend, and the solid blue arrows mark the melt-rock reaction-crystallization trend in orthopyroxene and clinopyroxene compositional variations.

Two types of variation trends are observed in orthopyroxene and clinopyroxene compositions from the melt-rock reaction experiments: the melting and reequilibration trend and the reaction-crystallization trend (Wang et al., 2013). The former is characterized by decreases of incompatible elements (e.g., TiO_2, Al_2O_3, and Na_2O) and a slight increase of Mg# in pyroxenes (dashed red arrows in Fig. 7), and the latter by gradual enrichments of the incompatible elements with a significant decrease of Mg# (blue arrows in Fig. 7). Compositions of orthopyroxene from the isothermal hydrous melt-rock reaction experiment BAH8 plot at the high-Mg# ends on the oxide-Mg# variation diagrams. Compositions of pyroxenes from the hydrous reactive crystallization experiments further expand the melt-rock reaction trend that are mainly

established by pyroxenes from the anhydrous reactive crystallization experiments of Tursack and Liang (2012) and Saper and Liang (2014) with Mg# down to lower than 70.

Figure 8 plots Cr# against Mg# and TiO_2 content in spinel from the melt-rock reaction experiments. Spinel from the hydrous reactive crystallization experiments is scattered in Cr# (6-55), consistent with the observed core-to-rim variations in spinels from the hydrous reactive crystallization experiments (inset in Fig. 3b). Spinels from the isothermal run BAH8 are plotted at the high-Cr# end of data from the hydrous experiments. Mg# (46-61) and TiO_2 content (0.19-0.40 wt%) in spinel from the hydrous experiments are relatively uniform, both lower than those in the anhydrous experiments.

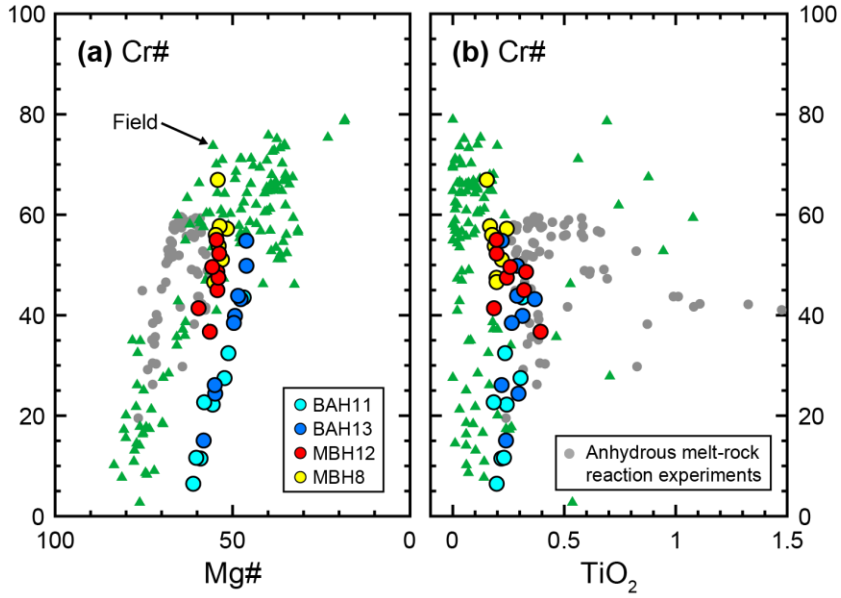

Figure 8. Variations of Cr# as a function of Mg# or TiO_2 abundance (in wt%) in spinel from melt-peridotite reaction experiments and those from field observations of amphibole-bearing mantle rocks (green triangles). Color circles are spinels in experiments from this study. Gray circles are spinels from anhydrous reaction experiments (PDET1, PDET1b, and PDET1c) of Turack and Liang (2012). Source of the field data are the same as in Fig. 6.

Figure 9 compares compositions of amphibole from this study with those from the melt-peridotite reaction experiments of Sen and Dunn (1994), Mallik et al. (2015), and Mandler and Grove (2016) that have low starting melt-to-peridotite ratios (gray triangles). Also shown in Fig. 9 are amphiboles from phase equilibrium experiments for hydrous basaltic and andesitic compositions (plus symbols). Compositions of amphibole from the melt-rock reaction experiments broadly vary along continuous trends (arrows), different from the phase equilibrium experiments which have relatively scattered amphibole compositions. Amphiboles from the low melt-to-peridotite ratio reaction experiments are plotted at the high-Mg# end (88-92) of the oxide vs. Mg# variation diagrams. Amphiboles in the peridotite and orthopyroxenite regions from our hydrous reaction experiments have lower Mg#, and those from the gabbronorite region have the lowest Mg#. Amphiboles from phase equilibrium studies have lower Al_2O_3 and higher SiO_2 than those from the melt-rock reaction experiments at a given Mg# (Figs. 9a and 9b), whereas they broadly overlap the melt-rock reaction trends in the CaO, TiO_2, Na_2O, and MnO vs. Mg# diagrams (Figs. 9c-9f).

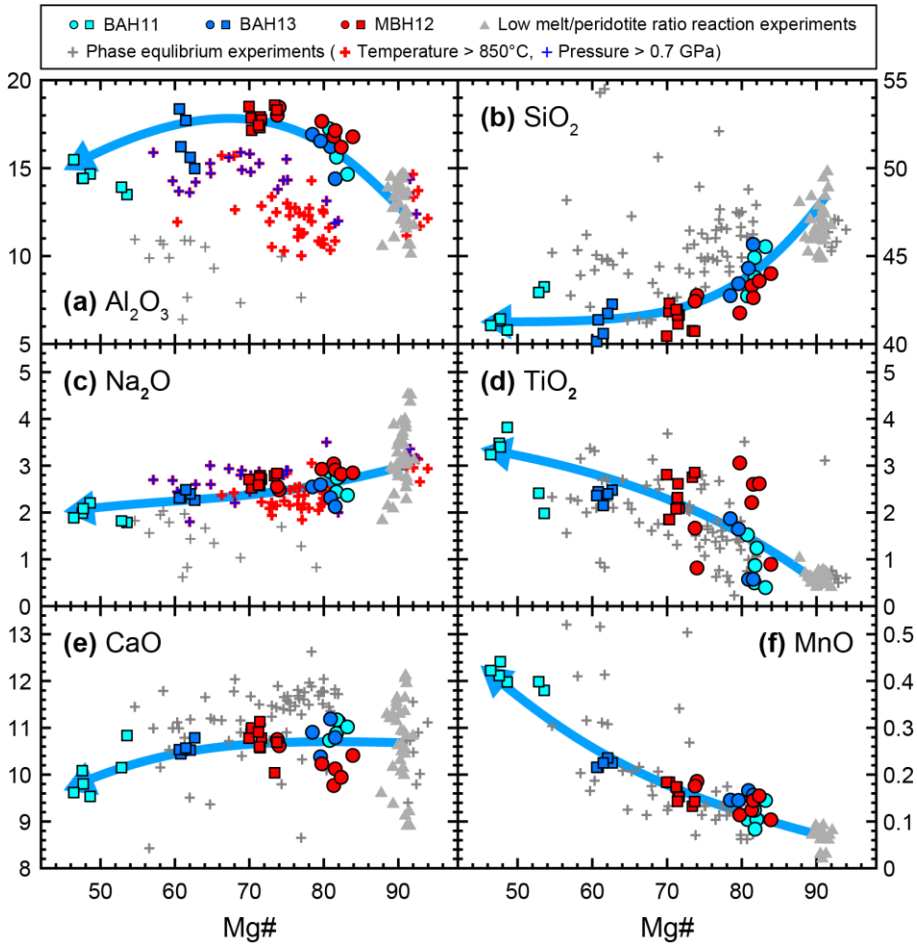

Figure 9. Variations of oxide abundances (in wt%) as a function of Mg# in amphibole from melt-peridotite reaction experiments (circles, squares, and triangles) and phase equilibrium experiments (plus symbols, Nicholls and Harris, 1980; Green and Pearson, 1985; Latourrette et al., 1995; Feig et al., 2006; Mercer and Johnston, 2008; Parat et al., 2008; Pietranik et al., 2009; Nandedkar et al., 2016). Circles are amphiboles in the amphibole-bearing orthopyroxenite and peridotite regions, and squares are those in the amphibole gabbronorite region in reaction experiments from this study (identical to those in Fig. 5). Triangles are amphiboles in the low melt-to-rock ratio reaction experiments (Sen and Dun 1994; Mallik et al. 2015; Mandler and Grove 2016). Blue arrows mark the amphibole compositional variation trends established by the melt-peridotite reaction experiments. Data from the phase equilibrium studies are discriminated by experimental temperature and pressure in (a) and (c).

Figure 10 compares plagioclase compositions from melt-rock reaction experiments with those from phase equilibrium experiments. Plagioclase compositions from the reaction experiments are generally low in An#, FeO and MgO contents than the phase equilibrium experiments except some experiments that were run at subsolidus conditions (Borghini et al., 2010; Fumagalli et al., 2017). Plagioclase from hydrous melt-rock reaction experiments has similar An# and Al_2O_3 and FeO contents to, but significantly lower MgO content than, those from anhydrous ones in Saper and Liang (2014) (Fig. 10c).

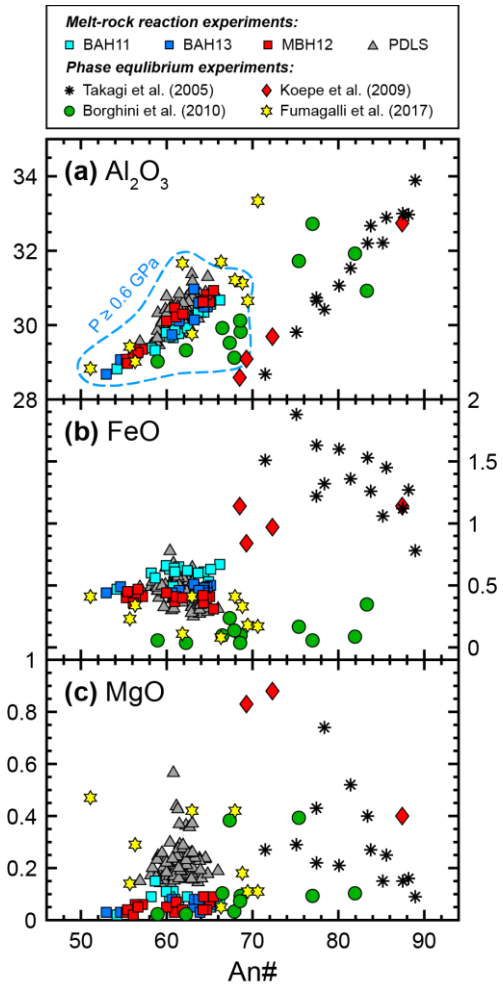

Figure 10. Variations of Al_2O_3, FeO, and MgO abundances (in wt%) vs. An# in plagioclase from melt-peridotite reaction experiments and phase equilibrium experiments. The reaction experiments include those from this study and the anhydrous ones (PDLS) from Saper and Liang (2014). The phase equilibrium experiments are from Takagi et al. (2005), Koepke et al. (2009), Borghini et al. (2010), and Fumagalli et al. (2017). The dashed field in (a) shows the range of data from experiments that were run at pressures greater than 0.6 GPa.

3.4. Origin of texture and mineral compositional variations

Texture of the melt-rock reaction experiments depends on major element composition and water content of the reacting melt, and P-T-t history. Reaction between the hydrous basaltic andesite and lherzolite at 1200°C and 1 GPa produced a high-porosity orthopyroxenite-dunite sequence (run BAH8 in Wang et al., 2016). The dunite is formed by hydrous melting of lherzolite, and the orthopyroxenite is formed by reaction between olivine and the interface melt with orthopyroxene as the liquidus phase (Fig. 11a). Oversaturation of orthopyroxene in the hydrous reacting melt leads to the crystallization of orthopyroxene upon subsequent cooling, forming the orthopyroxene oikocrysts in the peridotite (Figs. 3 and 11b). Clinopyroxene and amphibole are near-liquidus phases of interstitial melts in the peridotite and orthopyroxenite. Stability of clinopyroxene on the liquidus increases from hydrous basaltic andesite to hydrous basalt (e.g., Weaver et al., 2011). This explains the more abundant clinopyroxene in run MBH12 than in runs BAH11 and BAH13, and the replacement of orthopyroxene by clinopyroxene around the gabbronorite-orthopyroxenite interface in MBH12 (Figs. 3 and 11c). Orthopyroxene

and clinopyroxene are surrounded by amphiboles (Figs. 2, 3, and 11d), suggesting the delayed crystallization of the latter. In the anhydrous reactive crystallization experiments, clinopyroxene is the main phase crystallized during cooling (Tursack and Liang, 2012) and plagioclase is precipitated when melt infiltration is extensive (Saper and Liang, 2014). The presence of water in reacting melt in the hydrous reactive crystallization experiments stabilizes amphibole which crystallizes throughout the peridotite region (Fig. 3). Crystallization of amphibole is at the expenses of clinopyroxene and hydrous melt, resulting in the embayed clinopyroxenes in the peridotite and the small clinopyroxene inclusions near the rims of large amphiboles in the gabbronorite (Figs. 3 and 11d). The empty vesicles formed during quench represent water exsolved from interstitial melt upon cooling. Surface tension and capillary suction drive water to the porous olivine matrix. The euhedral shape of plagioclase grains in the gabbronorite region suggests that plagioclase is the last phase of crystallization.

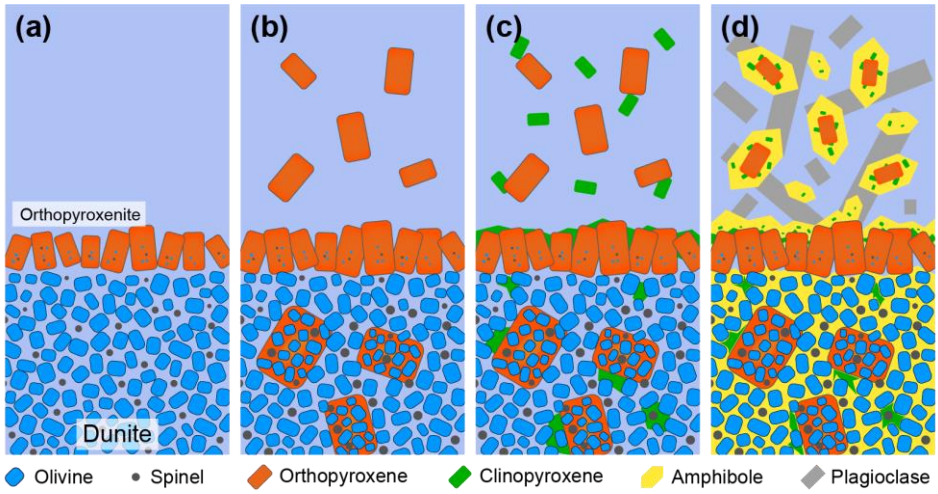

Figure 11. Schematic diagrams illustrating processes leading to the formation of amphibole-bearing gabbronorite – orthopyroxenite – peridotite sequence in the hydrous melt and lherzolite reactive crystallization experiments. (a) Formation of orthopyroxenite-dunite sequence by reaction between hydrous melt and peridotite at 1200°C (adapted from Wang et al., 2016). (b-d) Successive crystallizations of orthopyroxene, clinopyroxene, amphibole, and plagioclase during the step-cooling.

Mg# and NiO content in olivine are governed by extent of peridotite melting. The high degree of peridotite melting promoted by hydrous melt infiltration at 1200°C accounts for the higher Mg# and NiO contents in olivine from the hydrous experiments than those from the anhydrous ones (Fig. 6a). The hydrous reaction experiments were run at relatively low temperatures (1200°C with a cooling to 880°C) compared to the anhydrous ones (1300-1320°C with a cooling to 1200°C or 1050°C or without), which gives rise to the lower CaO in olivine, the lower CaO in orthopyroxene, and higher CaO in clinopyroxene from the hydrous experiments than those in the anhydrous ones (e.g., Brey and Köhler, 1990; Köhler and Brey, 1990, Figs. 6 and 7). Such relationship between temperature and CaO in olivine and pyroxenes has been also observed in previous melt-rock reaction studies (e.g., Wang et al., 2013, 2016; Saper and Liang, 2014). Step-cooling expands the temperature ranges of the runs and hence the larger ranges of Mg# in pyroxenes and Cr# in spinel along the melt-rock reaction trends in Figs. 7 and 8.

The variations in amphibole composition from the experimental studies can be attributed to the differences in temperature, pressure, and melt composition. From the low melt-to-rock

ratio reaction experiments (Sen and Dunn, 1994; Mallik et al., 2015; Mandler and Grove, 2016) to the peridotite and orthopyroxenite regions to the gabbronorite region in the present experiments, Mg# in amphibole decreases, in accordant with the difference in melt composition from which amphibole is crystallized (Fig. 9). The variation trends of TiO_2 and MnO versus Mg# in amphibole from the melt-rock reaction experiments are broadly similar to those from the phase equilibrium experiments (Figs. 9d and 9f), whereas Al_2O_3 and Na_2O in amphibole from the reaction experiments are generally higher than those from the phase equilibrium experiments. Al_2O_3 in amphibole increases with temperature (for tetrahedral Al) and pressure (for octahedral Al) (e.g., Spear, 1981; Ernst and Liu, 1998; Larocque and Canil, 2010), and Na_2O in amphibole increases with pressure (e.g., Ernst and Liu, 1998; Niida and Green, 1999). Amphibole from experiments run at high temperatures (> 850°C) or at high pressures (> 0.7 GPa) has relatively high Al_2O_3 content, and amphibole from experiments run at high pressures (> 0.7 GPa) has relatively high Na_2O content (Fig. 9). These temperature- and pressure-dependent Al_2O_3 and Na_2O variations are consistent with the grain-scale variations of amphibole composition: as temperature and pressure decrease during step-cooling, the amphibole grows with decreasing Al_2O_3 and Na_2O contents in the rim (Fig. S3). In spite of the numerous factors that control amphibole composition during melt-rock reaction, the laboratory melt-rock reaction experiments establish general variation trends (blue arrows in Figs. 9 and 12). As melt-rock reaction or diffusive exchange between reacting melt and minerals becomes extensive, Mg# and Na_2O in amphibole decrease, whereas MnO, TiO_2, and Al_2O_3 in amphibole increase.

Composition of plagioclase can be affected by temperature, pressure, and melt composition (Longhi et al., 1976; Namur et al., 2012; Faak et al., 2013). As demonstrated by Saper and Liang (2014), reaction of MORB with peridotite at a moderate pressure delays the crystallization of plagioclase. Presence of water also delays plagioclase crystallization in basalts (Takagi et al., 2005; Borghini et al., 2010; Namur et al., 2012). In our hydrous reactive crystallization experiments, plagioclase is the last mineral to crystallize. This explains the relatively low An# in plagioclase from these experiments, compared with that from the phase equilibrium studies (Fig. 10a). Because of the late-stage crystallization (i.e., from an evolved residual melt at low P and T), FeO and MgO contents in plagioclase from the reaction experiments are low, comparable to those from the subsolidus phase equilibrium experiments of Borghini et al. (2010) and Fumagalli et al. (2017) (Figs. 10b and 10c). In contrast, FeO and MgO contents in plagioclase from the phase equilibrium experiments of Takagi et al. (2005) and Koepke et al. (2005) are high (Figs. 10b and 10c), as it is the near-liquidus mineral in these experiments.

4. Geological applications

The experiments reported here and those in Tursack and Liang (2012), Saper and Liang (2014), and Wang et al. (2016) underscore the importance of water in the reacting melt in determining the lithology and mineral compositional variations produced by melt-rock reaction in the mantle. Hydrous basalts-peridotite reaction and in situ crystallization can produce a spatially associated amphibole-bearing peridotite and amphibole-bearing orthopyroxenite sequence. Because of the simplified experimental setup, the mass transfer mechanism may be different between melt-peridotite interaction in the laboratory experiments and those in nature (e.g., diffusion vs. advection). Extensive water infiltration into the powdered starting peridotite lead to partial melting and faster reaction. The rate of cooling in the experiments is likely faster than that takes place in nature. Nevertheless, the kinetics and compositional variation trends are

quite similar between the laboratory experiments and those in nature, because they are determined by chemical potential gradients of the major components and phase relationships in the hydrous basalt-peridotite system. The fast reaction and crystallization rates manifest grain-scale processes and help to develop chemical variations on the laboratory time scale and length scale. To assess the effect of hydrous melt-peridotite interaction in modifying composition and mineralogy of the lithospheric mantle, we compare mineral compositions obtained from laboratory melt-rock reaction experiments with those from the field in Figs. 6-9, and 12. Calculation of chemical formula and nomenclature of the amphibole supergroup follow the method described in Leake et al. (1997). We prefer to use this Si-Al-Na-K based amphibole classification in this study because abundances and substitution of these elements are important indications of melt composition and temperature and pressure conditions.

4.1. Olivine, pyroxenes and spinel in amphibole-bearing mantle rocks

Figures 6, 7 and 8 compare compositions of olivine, pyroxenes, and spinel obtained from laboratory melt-peridotite reaction experiments with those in the amphibole-bearing mantle rocks from the field. Compositional variations of these minerals from the field samples broadly follow the trends established by the melt-peridotite reaction experiments, although clinopyroxenes from the reaction experiments are lower in Mg# than the field data. The mismatch in Mg# between the experimental data and the field data are also observed in the amphibole compositions (Figs. 12b and 12e). These are in part due to the evolved nature of reacting melts and high melt-to-peridotite ratios in the experiments and the subsolidus state of the natural samples. In previous experimental studies (e.g., Morgan and Liang, 2005; Van den Bleeken et al., 2010; Tursack and Liang, 2012; Wang et al., 2013; Saper and Liang, 2014), common mismatches in CaO concentrations in olivine and pyroxenes were observed between field data and melt-rock reaction experimental data: clinopyroxenes are higher in CaO while olivines and orthopyroxenes are more depleted in CaO for the field data. These are attributed to subsolidus reequilibration of the field samples and the high temperature nature of the dissolution experiments (>1200°C). Figures 6 and 7 show that CaO contents in olivine and pyroxenes from the hydrous reaction experiments are close to those from the field observations, consistent with the low reaction and crystallization temperatures in these experiments (1200°C to 880°C).

4.2. Amphiboles from mantle xenoliths

Figures 12a-12c compare compositions of amphibole obtained from the laboratory experiments with those from mantle xenoliths. Amphiboles in the mantle xenoliths are mainly pargasite and edenite with a small population being Mg-hornblende and tremolite. The main composition range of amphibole in the mantle xenoliths overlaps that obtained from the melt-rock reaction experiments (gray fields). Harzburgite xenoliths in andesites from Avacha, Kamchatka (Bénard and Ionov, 2013) contain amphiboles in different lithological regions, including the host harzburgite, orthopyroxene-rich veins that have reaction texture with host harzburgite, and orthopyroxene-rich veins without reaction texture. The reaction texture between the orthopyroxene-rich veins and the host harzburgite is similar to that observed around the orthpyroxenite-peridotite interface in our experiments (Fig. 3). Amphiboles in the host harzburgite and those in the veins with reaction texture (dark green squares) are mainly pargasite and subordinately enenite and Mg-hornblende (Fig. 12a). Compositions of these amphiboles are mainly in the range defined by the melt-rock reaction experiments (gray fields). The textural and compositional features suggest that these veins were formed by reaction of peridotite and

hydrous melt in the lithospheric mantle (Bénard and Ionov, 2013). Amphiboles in the host harzburgite were likely crystallized from reacting melt that infiltrated into the peridotite. In contrast, the other type of orthopyroxene-rich veins crosscut the host harzburgite, and they have a straight contact with the host harzburgite. Amphiboles in these veins (light green squares) are mainly Mg-hornblende (Fig. 12a). They have low T-site Al, A-site Na, Ti abundances, and high Mg#, varying along a trend defined by some amphiboles from phase equilibrium experiments (thin green arrows in Fig. 12). The above evidence indicates that these veins are formed by direct crystallization of the host andesitic melt during the transport of xenoliths to the surface.

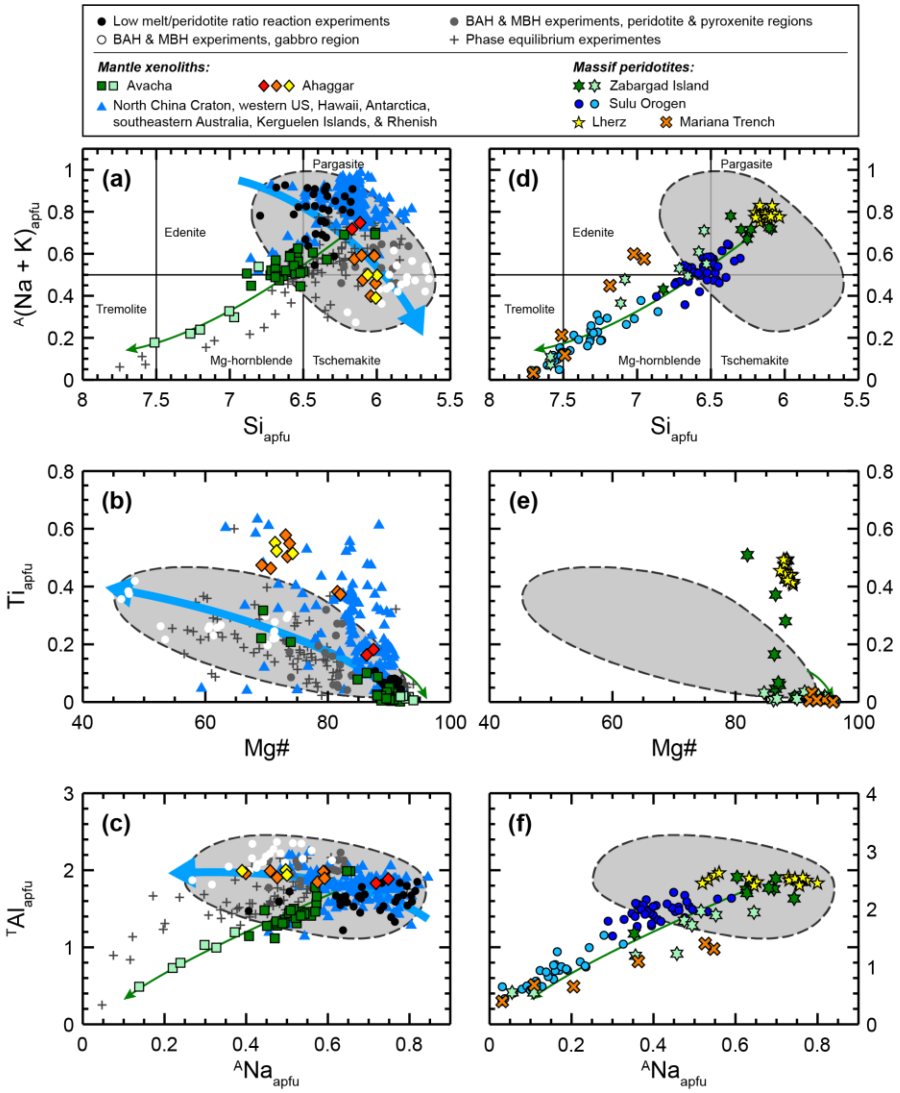

Figure 12. Plots of atomic compositions for amphiboles from the experiments and field observations of amphibole-bearing mantle xenoliths (a-c) and massif peridotite (d-f). Calculation of chemical formula and division of compositional boundaries (in a and d) follow Leake et al. (1997). The experimental data are shown as black dots (low melt-to-rock ration reaction experiments, shown in Fig. 9), gray dots (peridotite and pyroxenite regions in experiments from the present study), white dots (gabbronorite regions in experiments from the present study), and gray plus symbols (phase equilibrium experiments, shown in Fig 9). The gray fields show composition range of amphibole from melt-rock reaction experiments, and the thick blue arrows indicate the melt-rock reaction trend of amphibole compositional variation. Source of the field data are the same as in Fig. 6. Amphiboles in peridotite xenoliths and orthopyroxene-rich veins that have reaction texture with the host peridotite from Avacha are shown as dark green squares, and those in orthopyroxene-rich veins without reaction texture are shown as light green squares.

Amphiboles in peridotite xenoliths, amphibole-rich veins and amphibolite xenoliths, and amphibole megacrysts from Ahaggar are shown as red, orange, and yellow diamonds, respectively. Amphiboles from the other mantle xenoliths are shown as blue triangles. Amphiboles in spinel peridotites and the amphibole-bearing bands associate with secondary minerals in massif peridotites from Zabargad Island, are shown as dark green hexagons, and amphiboles in the mylonitic share zones are shown as light green hexagons. Amphibole cores and rims from the Sulu peridotites are shown as dark and light circles, respectively. Amphiboles in lherzolites and amphibolite veins from the Lherz massif are shown as yellow pentagrams, and those in serpentinized peridotites from Mariana Trench are shown as orange crosses. The thin green arrows indicate the compositional variation trend of amphiboles that were likely formed by crystallization of host magma of mantle xenolith or by hydrothermal alteration at shallower depths.

Different occurrences of amphiboles are also observed in a suit of mantle xenoliths and megacrysts entrained by basalts from Ahaggar, southern Algeria (Dautria et al., 1987). Amphiboles are present in peridotites with amphibole-rich veins, amphibolites, and as megacrysts in the host basalt. Amphiboles are anhedral grains interstitial to anhydrous minerals in the peridotites and oikocrysts that have chadacrysts of anhydrous minerals in the amphibole-rich veins and amphibolites. Although amphibolite is not formed in the hydrous melt-rock reaction experiments, the poikilitic texture of amphibole in the Ahaggar xenoliths is similar to that observed in the peridotite region in the experiments (Fig. 2). Furthermore, amphiboles in the Ahaggar xenoliths with different occurrences show a compositional variation along the trend defined by the melt-rock reaction experiments (thick blue arrows in Fig. 12). Amphiboles in the peridotites (red diamonds) are high in Mg# and low in Ti (Fig. 12b), similar to those in ultramafic regions from our experiments (gray dots) and the low melt-to-rock ratio experiments (black dots). Amphiboles in the amphibole-rich veins and amphibolites (orange diamonds) have low Mg# and high Ti abundance (Fig. 12b), similar to the amphibole megacrysts in the host basalt (yellow diamonds) and those in the gabbronorite region of our experiments (white dots). The variations in occurrence and composition suggest that amphiboles in the Ahaggar peridotites and amphibolites were formed by reactive crystallization when hydrous melts infiltrate peridotite, and the amphibole megacrysts were crystallized from the reacted melt (Dautria et al., 1987). The reaction trend is also observed in the amphibole-bearing lherzolites from Victoria Land, Antarctica: amphibole disseminated in peridotite has a higher Mg# and a lower Ti abundance than that in the amphibole veins, suggestive of melt-rock reaction origin of the amphiboles with different melt-to-rock ratios (Coltorti et al., 2004).

4.3. Amphiboles from massif peridotites

Figures 12d-12f compare the experimental amphibole compositions with those from massif peridotites. The massif peridotites from Zabargad Island, Red Sea contain amphiboles interstitial to olivines in spinel peridotite, in bands associated with secondary spinel between bands of olivines, and in mylonitic shear zones (Agrinier et al., 1993). Massif peridotites from the Sulu Orogenic Belt, eastern China have amphiboles with core-to-rim compositional variation, and inclusions of olivine, serpentine and spinel (Li et al., 2018). The peridotite sample from the Lherz massif has an amphibolite vein. Modal abundance of amphibole increases from the host peridotite towards the vein (Zanetti et al., 1996). Massif peridotite samples from the island arc at Mariana Trench are serpentinized and contain tremolite, hornblende, and enenite (Fig. 12d) (Ohara and Ishii, 1998). Compositionally, amphiboles in the spinel peridotite and the secondary bands from Zabargad (dark green hexagons in Figs. 12d-12f), amphibole cores from Sulu (dark blue circles), and amphiboles from Lherz (yellow pentagrams) are mainly in the composition range of the melt-rock reaction experiments. This is consistent with the occurrences that these

amphiboles are interstitial or associated with secondary minerals, and supports the origin that they are from by reaction of peridotite with hydrous melts (e.g., Agrinier et al., 1993; Zanetti et al., 1996). Amphiboles in the mylonitic shear zones in the massif peridotites from Zabargad (light green hexagons in Figs. 12d-12f), amphibole rims in the Sulu orogenic peridotite (light blue circles in Figs. 12d-12f), and amphiboles in the serpentinized peridotites from Mariana Trench (orange crosses, Ohara and Ishii, 1998) vary along the trend that is different from that defined by the melt-rock reaction experiments (thin green arrows in Fig. 12d-12f). The compositional variation and the occurrences of these amphiboles indicate that they were formed by processes such as hydrothermal alteration (fluid-rock reaction) when the peridotites have emplaced or exhumed at shallow depths (Agrinier et al., 1993; Ohara and Ishii, 1998; Li et al., 2018).

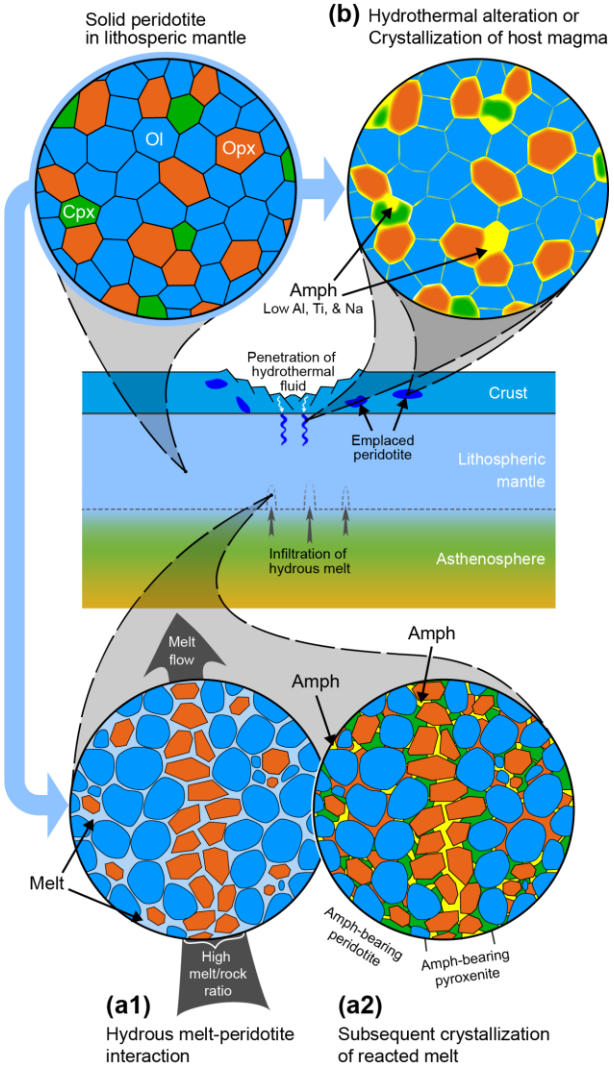

Figure 13. Schematic diagrams illustrating scenarios where amphiboles are formed in the lithospheric mantle. (a1) and (a2) show the processes leading to the formation of amphibole-bearing peridotite and pyroxenite by hydrous melt-peridotite interaction. Hydrous melt infiltration initiates partial melting of the peridotite in lithospheric mantle. Reaction between the hydrous melt and the peridotite forms orthopyroxene-depleted peridotite and orthopyroxene vein or dike (a1). As the peridotite cooled, the interstitial melts crystallize clinopyroxene and amphibole with composition varying along the trends established by the melt-rock reaction experiments forming amphibole-bearing peridotite and pyroxenite (a2). (b) shows the formation of amphibole in peridotite by metamorphism. Hydrothermal

fluids penetrate peridotite at the crust-mantle boundary or in the lower crust after peridotite emplacement forming amphibole with high Mg#, SiO_2, and CaO and low Al_2O_3, TiO_2, and Na_2O contents (magenta trends in Fig. 13). Ol = olivine; Opx = orthopyroxene; Cpx = clinopyroxene; Amph = amphibole.

4.4. Formation mechanisms of amphibole-bearing mantle rocks

The amphibole-bearing pyroxenite and amphibole-bearing peridotite that formed in the hydrous melt-peridotite reaction experiments are similar to a number of field observations in terms of texture, lithology, and mineral compositions, indicating that these field amphiboles are likely formed by hydrous melt-peridotite interaction. The schematic diagram in Fig 13 summarizes mechanisms through which various amphiboles are formed in the lithospheric mantle. Infiltration of hydrous melts may be focused either by means of hydro-fracturing or reaction induced infiltration instability similar to the one that produces replacive dunite in the mantle section of ophiolite (e.g., Kelemen et al., 1997). When a hydrous melt (or fluid) infiltrate the lithospheric mantle along pressure gradients or fractures, it may induce partial melting of the surrounding peridotite. Further reaction between the hydrous melt and the partially molten peridotite produces a melt-bearing orthopyroxenite vein (Fig. 13a1, Wang et al., 2016). A new generation of clinopyroxene and amphibole then precipitate from the trapped interstitial melts as the peridotite is cooled or water in melt is released (by diffusion or change of pressure). The precipitation may occur in the partially molten peridotite and the melt-bearing orthopyroxenite, forming an amphibole-bearing peridotite and an amphibole-bearing pyroxenite, respectively (Fig. 13a2). It can be inferred that the precipitation may form an amphibole-rich lithology in reaction zone where the proportion of hydrous melt is high. The amphibolites from Ahaggar (Dautria et al., 1987) and amphibole veins in lherzolites from Victoria Land (Coltorti et al., 2004) may represent such examples.

However, not all amphiboles in mantle rocks are formed by melt-rock reaction. Compositions of some amphiboles in natural samples are different from those produced by the melt-rock reaction experiments (Fig. 12). These amphiboles grow as rims of amphiboles formed by melt-rock reaction (e.g., Li et al., 2018), occur in veins that show not textural evidence of reaction with the host peridotites (e.g., Agrinier et al., 1993; Bénard and Ionov, 2013), or present in peridotite with evidence of hydrothermal alteration (e.g., Ohara and Ishii, 1998). They are likely formed by processes such as crystallization of host magma of mantle xenoliths or hydrothermal alteration after emplacement or exhumation of peridotite massifs at crustal depths (Fig. 13b).

5 Conclusions

The role of hydrous melt-peridotite reaction in the formation of amphibole-bearing mantle rocks is examined by reacting spinel lherzolite with a hydrous basaltic andesite and a hydrous MORB (with 4 wt% water in the melts) in Au-Pd capsules using the reaction couple method. The experiments include a reaction at 1200°C and 1 GPa and a further reaction/crystallization through a series of step cooling to 880°C and 0.8 GPa. Results of the hydrous melt-peridotite reaction experiments together with those conducted under anhydrous conditions are used to deduce processes leading to the formation of amphibole in mantle rocks. The main conclusions of this study are as follows:

1. Reaction between hydrous basaltic melt and lherzolite followed by in situ crystallization produces an amphibole gabbronorite, amphibole-bearing orthopyroxenite, and amphibole-bearing peridotite sequence.
2. A high-porosity orthopyroxenite-dunite sequence is formed in the reaction at 1200°C. Crystallization of orthopyroxene continues at the early stages of cooling, followed by clinopyroxene, and finally amphibole in the peridotite and orthopyroxenite.
3. Lithology, texture, and mineral compositional variation are key features that can be used to deduce the origin of amphiboles in peridotites and pyroxenites.
4. Similarities in these key features between the experiments reported in this study and those observed in amphibole-bearing mantle xenoliths and massif peridotites underscore the importance of hydrous melt-peridotite reaction and in situ crystallization in the formation of amphiboles in these mantle rocks.
5. Texture and compositional variations of some amphiboles from the field are distinct from those obtained from the melt-peridotite reaction experiments, including the low Ti, Al, and Na abundances. These amphiboles are likely formed by crystallization of xenoliths' host magma and hydrothermal alterations at shallow depths.

Acknowledgments

We thank Joseph Boesenberg for assistance in microprobe analyses. This work was supported by grant from National Natural Science Foundation of China (41602043), Key Basic Research Program of China (2015CB856101), and grants from US National Science Foundation (EAR-1624516 and OCE-1852088). Electron microprobe data are archived at Mendeley Data (http://dx.doi.org/10.17632/895f6y8chd.1).

References

Agrinier, P., Mével, C., Bosch, D., & Javoy, M. (1993). Metasomatic hydrous fluids in amphibole peridotites from Zabargad island (Red Sea). *Earth and Planetary Science Letters*, 120, 187–205

Barr, J. A., & Grove, T. L. (2010). Au Pd Fe ternary solution model and applications to understanding the fO_2 of hydrous, high-pressure experiments. *Contributions to Mineralogy and Petrology*, 160, 631–643

Beck, A. R., Morgan, Z. T., Liang, Y., & Hess, P. C. (2006). Dunite channels as viable pathways for mare basalt transport in the deep lunar mantle. *Geophysical research letters*, 33, L01202

Bénard, A., & Ionov, D. A. (2013). Melt– and fluid–rock interaction in supra-subduction lithospheric mantle: Evidence from andesite-hosted veined peridotite xenoliths. *Journal of Petrology*, 54(11), 2339–2378

Bonadiman, C., Nazzareni, S., Coltorti, M., Comodi, P., Giuli, G., & Faccini, B. (2014). Crystal chemistry of amphiboles: Implications for oxygen fugacity and water activity in lithospheric mantle beneath Victoria land, Antarctica. *Contributions to Mineralogy and Petrology*, 167, 1–17

Borghini, G., Fumagalli, P., & Rampone, E. (2010). The stability of plagioclase in the upper mantle: subsolidus experiments on fertile and depleted lherzolite. *Journal of Petrology*, 51, 229–254

Brey, G. P., & Köhler, T. P. (1990) Geothermobarometry in four-phase lherzolites II. New thermobarometers, and practical assessment of existing thermobarometers. *Journal of Petrology* 31, 1353-1378

Carroll, M. R., & Wyllie, P. J. (1989). Experimental phase relations in the system tonalite-peridotite-H_2O at 15 kbar: Implications for assimilation and differentiation processes near crust-mantle boundary. *Journal of Petrology*, 30,1351–1382

Clague, D. A., Bohrson, W. A. (1991). Origin of xenoliths in the trachyte at Puu Waawaa, Hualapai volcano, Hawaii. *Contributions to Mineralogy and Petrology*, 108, 439–452

Coltorti, M., Beccaluva, L., Bonadiman, C., Faccini, B., Ntaflos, T., & Siena, F. (2004). Amphibole genesis via metasomatic reaction with clinopyroxene in mantle xenoliths from Victoria land, Antarctica. *Lithos*, 75, 115–139

Daines, M. J., Kohlstedt, D. L. (1994). The transition from porous to channelized flow due to melt/rock reaction during melt migration. *Geophysical Research Letters*, 21, 145–148

Dautria, J. M., Liotard, J. M., Cabanes, N., Girod, M., & Briqueu, L. (1987). Amphibole-rich xenoliths and host alkali basalts: Petrogenetic constraints and implications on the recent evolution of the upper mantle beneath Ahaggar (Central Sahara, Southern Algeria). *Contributions to Mineralogy and Petrology*, 95, 133–144

Ernst, W. G., & Liu, J. (1998). Experimental phase-equilibirium study of Al- and Ti-contents of calcic amphibole in MORB-A semiquantitative thermobarometer. *American Mineralogist*, 83, 952–969.

Faak, K., Chakraborty, S., & Coogan, L. A. (2013). Mg in plagioclase: experimental calibration of a new geothermometer and diffusion coefficients. *Geochimica et Cosmochimica Acta*, 123, 195–217

Feig, S. T., Koepke, J., & Snow, J. E. (2006). Effect of water on tholeiitic basalt phase equilibria: An experimental study under oxidizing conditions. *Contributions to Mineralogy and Petrology*, 152, 611–638

Francis, D. M. (1976a). Amphibole pyroxenite xenoliths: cumulate or replacement phenomena from the upper mantle, Nunivak island, Alaska. *Contributions to Mineralogy and Petrology*, 58, 51–61

Francis, D. M. (1976b). The origin of amphibole in lherzolite xenoliths from Nunivak island, Alaska. *Journal of Petrology*, 17, 357–378

Frey, F. A., & Prinz, M. (1978). Ultramafic inclusions from San Carlos, Arizona: Petrologic and geochemical data bearing on their petrogenesis. *Earth and Planetary Science Letters*, 38, 129–176

Fumagalli, P., Borghini, G., Rampone, E., & Poli, E. (2017). Experimental calibration of Forsterite–Anorthite–Ca-Tschermak–Enstatite (FACE) geobarometer for mantle peridotites. *Contributions to Mineralogy and Petrology*, 172(6), 38

Green, T. H., & Pearson, N. J. (1985). Experimental determination of REE partition coefficients between amphibole and basaltic to andesitic liquids at high pressure. *Geochimica et Cosmochimica Acta*, 49, 1465–1468

Ishimaru, S., Arai, S., Ishida, Y., Shirasaka, M., & Okrugin, V. M. (2007). Melting and multi-stage metasomatism in the mantle wedge beneath a frontal arc inferred from highly depleted peridotite xenoliths from the Avacha volcano, Southern Kamchatka. *Journal of Petrology*, 48(2), 395–433

Johnston, A. D., & Wyllie, P. J. (1989). The system tonalite-peridotite-H_2O at 30 kbar, with applications to hyperdization in subduction zone magmatism. *Contributions to Mineralogy and Petrology*, 102, 257–264

Kelemen, P. B., Joyce, D. B., Webster, J. D., & Holloway, J. R. (1990). Reaction between ultramafic rock and fractionating basaltic magma II. Experimental investigation of reaction between olivine tholeiite and harzburgite at 1150–1050°C and 5 kb. *Journal of Petrology*, 31, 99–134

Kelemen, P. B., Hirth, G., Shimizu, N., Spiegelman, M., & Dick, H. J. B. (1997). A review of melt migration processes in the adiabatically upwelling mantle beneath oceanic spreading ridges. *Philosophical Transactions Mathematical Physical and Engineering Sciences*, 355, 283–318

Koepke, J., Schoenborn, S., Oelze, M., Wittmann, H., Feig, S. T., Hellebrand, E., Boudier, F., & Schoenberg, R. (2009). Petrogenesis of crustal wehrlites in the Oman ophiolite: Experiments and natural rocks. *Geochemisty Geophysics Geosystems*, 10, Q10002

Köhler, T. P., & Brey, G. P. (1990). Calcium exchange between olivine and clinopyroxene calibrated as a geothermobarometer for natural peridotites from 2 to 60 kb with applications. *Geochimica et Cosmochimica Acta*, 54, 2375–2388

Lambart, S., Laporte, D., & Schiano, P. (2009). An experimental study of focused magma transport and basalt–peridotite interactions beneath mid-ocean ridges: Implications for the generation of primitive MORB compositions. *Contributions to Mineralogy and Petrology*, 157, 429–451

Lambart, S., Laporte, D., Provost, A. & Schiano P. (2012). Fate of pyroxenite-derived melts in the peridotitic mantle: thermodynamic and experimental constraints. *Journal of Petrology*, 53, 451–476

Larocque, J., & Canil, D. (2010). The role of amphibole in the evolution of arc magmas and crust: the case from the Jurassic bonanza arc section, Vancouver Island, Canada. *Contributions to Mineralogy and Petrology*, 159, 475–492

Latourrette, T., Hervig, R. L., & Holloway, J. R. (1995). Trace element partitioning between amphibole, phlogopite, and basanite melt. *Earth and Planetary Science Letters*, 135, 13–30

Leake, B. E., Wooley, A. R., Arps, C. E., Birch, W. D., Gilbert, M. C., Grice, J. D., Hawthorne, E. C., Kato, A., Kisch, HJ., Krivovichev, V. G., Linthout, K., Laird, J., Maresch, W. V., Nickel, E. H., Schumacher, J. C., Smith, D. C., Stephenson, N. C. N., Whittaker, E. J. W., & Guo., Y., (1997). Nomenclature of amphiboles; report of the Subcommittee on amphiboles of the International Mineralogical Association Commission on New Minerals and Mineral Names. *European Journal of Mineralogy*, 9, 623–651

Li, H., Chen, R., Zheng, Y., Hu, Z., & Xu, L. (2018). Crustal metasomatism at the slab-mantle interface in a continental subduction channel: Geochemical evidence from orogenic peridotite in the Sulu Orogen. *Journal of Geophysical Research: Solid Earth*, 123, 2174–2198

Longhi, J., Walker, D., & Hays, F. (1976). Fe and Mg in plagioclase. Proceedings of the 7th Lunar Science Conference, Houston, TX, 15–19, March. pp, 1281–1300

Mallik, A., Nelson, J., & Dasgupta, R. (2015). Partial melting of fertile peridotite fluxed by hydrous rhyolitic melt at 2–3 GPa: Implications for mantle wedge hybridization by sediment melt and generation of ultrapotassic magmas in convergent margins. *Contributions to Mineralogy and Petrology*, 169, 1–24

Mandler, B. E., & Grove, T. L. (2016). Controls on the stability and composition of amphibole in the Earth's mantle. *Contributions to Mineralogy and Petrology*, 171, 68

Mercer, C. N., & Johnston, A. D. (2008). Experimental studies of the P–T–H_2O near-liquidus phase relations of basaltic andesite from North Sister Volcano, High Oregon Cascades: Constraints on lower-crustal mineral assemblages. *Mineralogy and Petrology*, 155, 571–592

Moine, B. N., Grégoire, M., O'Reilly, S. Y., Sheppard, S. M. F., & Cottin, J. Y. (2001). High field strength element fractionation in the upper mantle: Evidence from amphibole-rich composite mantle xenoliths from the Kerguelen Islands (Indian Ocean). *Journal of Petrology*, 42, 2145–2167

Morgan, Z., & Liang, Y. (2003). An experimental and numerical study of the kinetics of harzburgite reactive dissolution with applications to dunite dike formation. *Earth and Planetary Science Letters*, 214, 59–74

Morgan, Z., & Liang, Y. (2005). An experimental study of the kinetics of lherzolite reactive dissolution with applications to melt channel formation. *Contributions to Mineralogy and Petrology*, 150, 369–385

Namur, O., Charlier, B., Toplis, M. J., & Auwera, J. V. (2012). Prediction of plagioclase-melt equilibria in anhydrous silicate melts at 1-Atm. *Contributions to Mineralogy and Petrology*, 163, 133–150

Nandedkar, R. H., Hürlimann, N., Ulmer. P., & Müntener, O. (2016). Amphibole–melt trace element partitioning of fractionating calc-alkaline magmas in the lower crust: An experimental study. *Contributions to Mineralogy and Petrology*, 171, 71

Nicholls, I. A., & Harris, K. L. (1980). Experimental rare earth element partition coefficients for garnet, clinopyroxene and amphibole coexisting with andesitic and basaltic liquids. *Geochimica et Cosmochimica Acta*, 44, 287–308

Niida, K., & Green, D. H. (1999). Stability and chemical composition of pargasitic amphibole in morb pyrolite under upper mantle conditions. *Contributions to Mineralogy and Petrology*, 135, 18–40.

Ohara, Y., & Ishii, T. (1998). Peridotites from the southern Mariana forearc: Heterogeneous fluid supply in mantle wedge. *Island Arc*, 7, 541–558

O'Reilly, S. Y., Griffin, W. L., & Ryan, C. G. (1991). Residence of trace elements in metasomatized spinel lherzolite xenoliths: A proton-microprobe study. *Contributions to Mineralogy and Petrology*, 109, 98–113

Parat, F., Holtz, F., & Feig, S. (2008). Pre-eruptive conditions of the Huerto andesite (Fish Canyon system, San Juan volcanic field, Colorado): Influence of volatiles (C–O–H–S) on phase equilibria and mineral composition. *Journal of Petrology*, 49, 911–935

Pietranik, A., Holtz, F., Koepke, J., & Puziewicz, J. (2009). Crystallization of quartz dioritic magmas at 2 and 1 kbar: Experimental results. *Mineralogy and Petrology*, 97, 1–21

Powell, W., Zhang, M., O'Reilly, S. Y., & Tiepolo, M. (2004). Mantle amphibole trace-element and isotopic signatures trace multiple metasomatic episodes in lithospheric mantle, Western Victoria, Australia. *Lithos*, 75(1), 141–171

Rapp, R. P., Shimizu, N., Norman, M. D., & Applegate, G. S. (1999). Reaction between slab-derived melts and peridotite in the mantle wedge: experimental constraints at 3.8 GPa. *Chemical Geology*, 160, 335–356

Saper, L., & Liang, Y. (2014). Formation of plagioclase-bearing peridotite and plagioclase-bearing wehrlite and gabbro suite through reactive crystallization: An experimental study. *Contributions to Mineralogy and Petrology*, 167, 985

Sekine, T., & Wyllie, P. J. (1983). Experimental simulation of mantle hybridization in subduction zones. *The Journal of Geology*, 91, 511–528

Sen, C., & Dunn, T. (1994). Experimental modal metasomatism of a spinel lherzolite and the production of amphibole-bearing peridotite. *Contributions to Mineralogy and Petrology*, 119, 422–432

Spear, F. J. (1981). An experimental study of hornblende stability and compositional variability in amphibole. American Journal of Science 281, 697–734.

Takahashi, E., & Nakajima, K. (2002). Melting process in the Hawaiian plume: an experimental study. *American Geophysical Union Monograph*, 128, 403–418

Takagi, D., Sato, H., & Nakagawa, M. (2005). Experimental study of a low-alkali tholeiite at 1–5 kbar: optimal condition for the crystallization of high-An plagioclase in hydrous arc tholeiite. *Contributions to Mineralogy and Petrology*, 149, 527–540

Tursack, E., & Liang, Y. (2012). A comparative study of melt-rock reactions in the mantle: Laboratory dissolution experiments and geological field observations. *Contributions to Mineralogy and Petrology*, 163, 861–876

Van den Bleeken, G., Muntener, O., & Ulmer, P. (2010). Reaction processes between tholeiitic melt and residual peridotite in the uppermost mantle: An experimental study at 0.8 GPa. *Journal of Petrology*, 51, 153–183

Van den Bleeken, G., & Muntener, O., Ulmer, P. (2011). Melt variability in percolated peridotite: An experimental study applied to reactive migration of tholeiitic basalt in the upper mantle. *Contributions to Mineralogy and Petrology*, 161, 921–945

Wang, C., Liang, Y., Xu, W., & Dygert, N. (2013). Effect of melt composition on basalt and peridotite interaction: laboratory dissolution experiments with applications to mineral compositional variations in mantle xenoliths from the North China Craton. *Contributions to Mineralogy and Petrology*, 166, 1469–1488

Wang, C., Liang, Y., Dygert, N., & Xu, W. (2016). Formation of orthopyroxenite by reaction between peridotite and hydrous basaltic melt: An experimental study. *Contributions to Mineralogy and Petrology*, 171, 77

Weaver, S. L., Wallace, P. J., & Johnston, A. D. (2011). A comparative study of continental vs. intraoceanic arc mantle melting: experimentally determined phase relations of hydrous primitive melts. *Earth and Planetary Science Letters*, 308, 97–106

Wilshire, H. G., Calk, L. C., & Schwarzman, E. C. (1971). Kaersutite — a product of reaction between pargasite and basanite at Dish Hill, California. *Earth and Planetary Science Letters*, 10, 281–284

Wilshire, H. G., Pike, J. E. N., Meyer, C. E., & Schwarzman, E. C. (1980). Amphibole-rich veins in lherzolite xenoliths, Dish Hill and Deadman Lake, California. *American Journal of Science*, 280(A), 576–593

Witt, G., & Seck, H. A. (1989). Origin of amphibole in recrystallized and porphyroclastic mantle xenoliths from the Rhenish Massif: Implications for the nature of mantle metasomatism. *Earth and Planetary Science Letters*. 91(3), 327–340

Witt-Eickschen, G., Seck, H. A., Mezger, K., Eggins, S.M., & Altherr, R. (2003). Lithospheric mantle evolution beneath the Eifel (Germany): Constraints from Sr–Nd–Pb isotopes and trace element abundances in spinel peridotite and pyroxenite xenoliths. *Journal of Petrology*, 44(6), 1077–1095

Xu, W., Yang, D., Gao, S., Pei, F., & Yu, Y. (2010). Geochemistry of peridotite xenoliths in early cretaceous High-Mg# diorites from the central orogenic block of the North China Craton: The nature of Mesozoic lithospheric mantle and constraints on lithospheric thinning. *Chemical Geology*, 270, 257–273

Xu, Y., & Bodinier, J. (2004). Contrasting enrichments in high- and low-temperature mantle xenoliths from Nushan, Eastern China: Results of a single metasomatic event during lithospheric accretion? *Journal of Petrology*, 45, 321–341

Yaxley, G. M., & Green, D. H. (1998). Reactions between eclogite and peridotite: mantle refertilisation by subduction of oceanic crust. *Schweizerische Mineralogische Und Petrographische Mitteilungen*, 78, 243–255

Zanetti, A., Vannucci, R., Bottazzi, P., Oberti, R., & Ottolini, L. (1996). Infiltration metasomatism at Lherz as monitored by systematic ion-microprobe investigations close to a hornblendite vein. *Chemical Geology*, 134, 113–133

Journal of Geophysical Research: Solid Earth

Supporting Information for

Formation of Amphibole-Bearing Peridotite and Amphibole-Bearing Pyroxenite through Hydrous Melt-Peridotite Reaction and In Situ Crystallization: An Experimental Study

Chunguang Wang[1, 2, *], Yan Liang[2], and Wenliang Xu[1]

1. College of Earth Sciences, Jilin University, Changchun 130061, China

2. Department of Earth, Environmental and Planetary Sciences, Brown University, Providence, RI 02912, USA

*Corresponding author: Chunguang Wang (c_wang@jlu.edu.cn)

Contents of this file

Introduction

This file includes figures and data supporting the main text:

- Figure S1 displays BSE images for BAH11;
- Figure S2-S3 show core-to-rim compositional variations in orthopyroxene, amphibole, and plagioclase grains;
- Figure S4-S8 plot olivine, clinopyroxene, and spinel compositions as a function of distance from the gabbronorite-orthopyroxenite interface;
- Tables S1-S3 present electron microprobe data of experimental results.

  Oxide abundances are in wt%, and distances are in μm; Total Fe as FeO; NA = not analyzed; ND = not detected; X = distance from gabbronorite-orthopyroxenite interface (X > 0 in the orthopyroxenite and peridotite regions, X < 0 in the gabbronorite region); D = distance from the center of mineral grain. Mg# = 100 × Mg/(Mg + Fe), in molar; Cr# = 100 × Cr/(Cr + Al), in molar; An# = 100 × Ca/(Ca + Na), in molar.

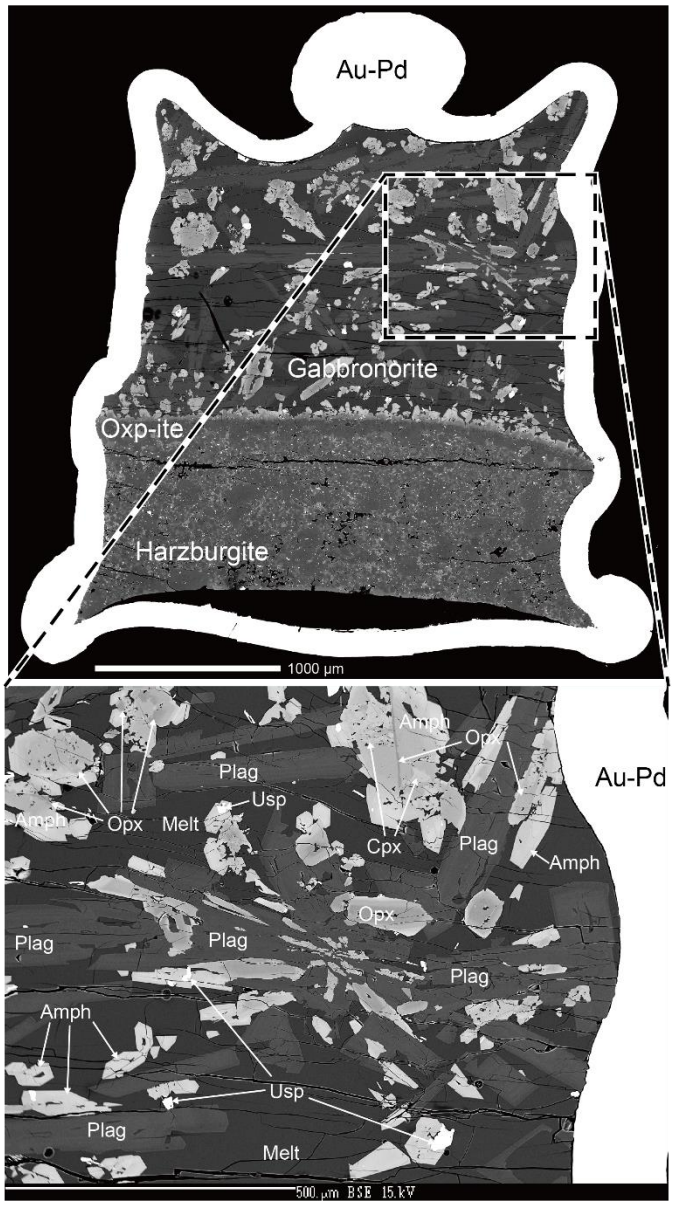

Figure S1. BSE images showing the experimental charge (upper) and a close-up view of the gabbronorite region (lower) of BAH11 (hydrous basaltic andesite vs. lherzolite, 3 h reaction). Opx-ite = orthopyroxenite; Opx = orthopyroxene; Cpx = clinopyroxene; Amph = amphibole; Plag = plagioclase; Usp = Ulvöspinel.

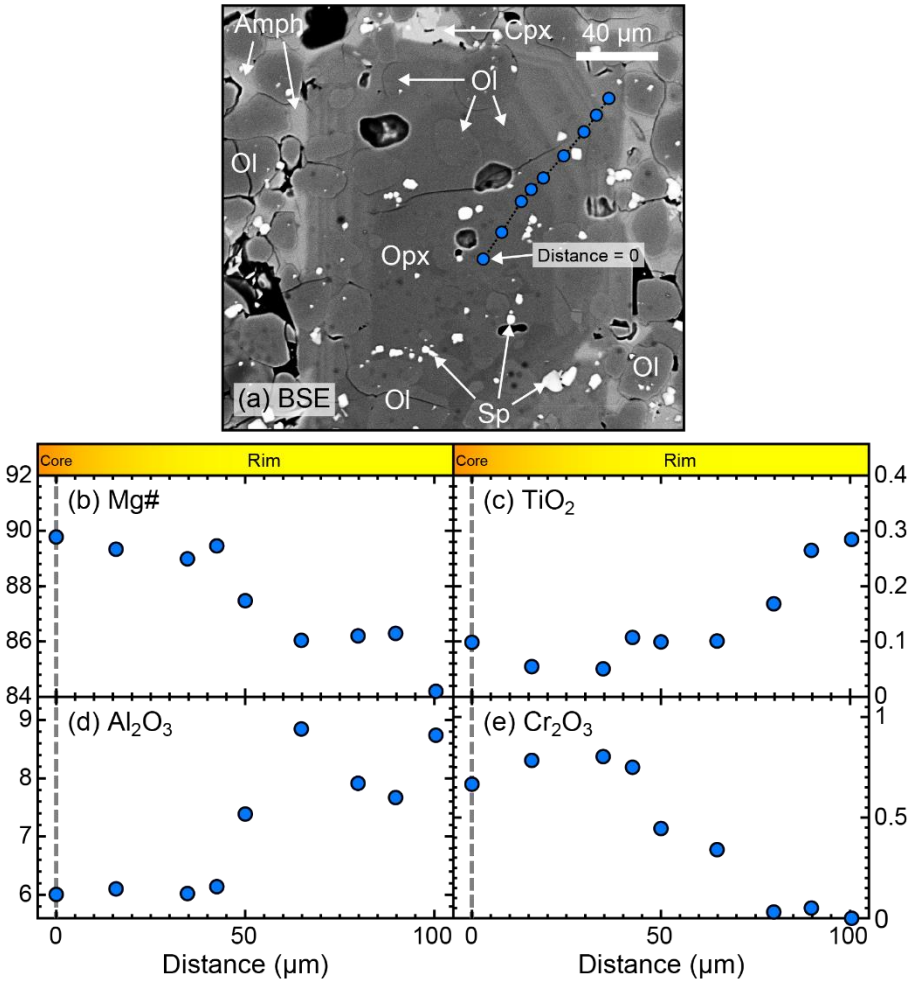

Figure S2. BSE image and electron microprobe data showing the chemical zoning of an orthopyroxene grain. (a) Core-to-rim zoned orthopyroxene in peridotite from BAH13. (b-e) Variations of Mg# and oxide abundances (in wt%) in orthopyroxene as a function of distance from the orthopyroxene core. Blue circles in (a) mark positions of the probe analyses plotted in (b-e).

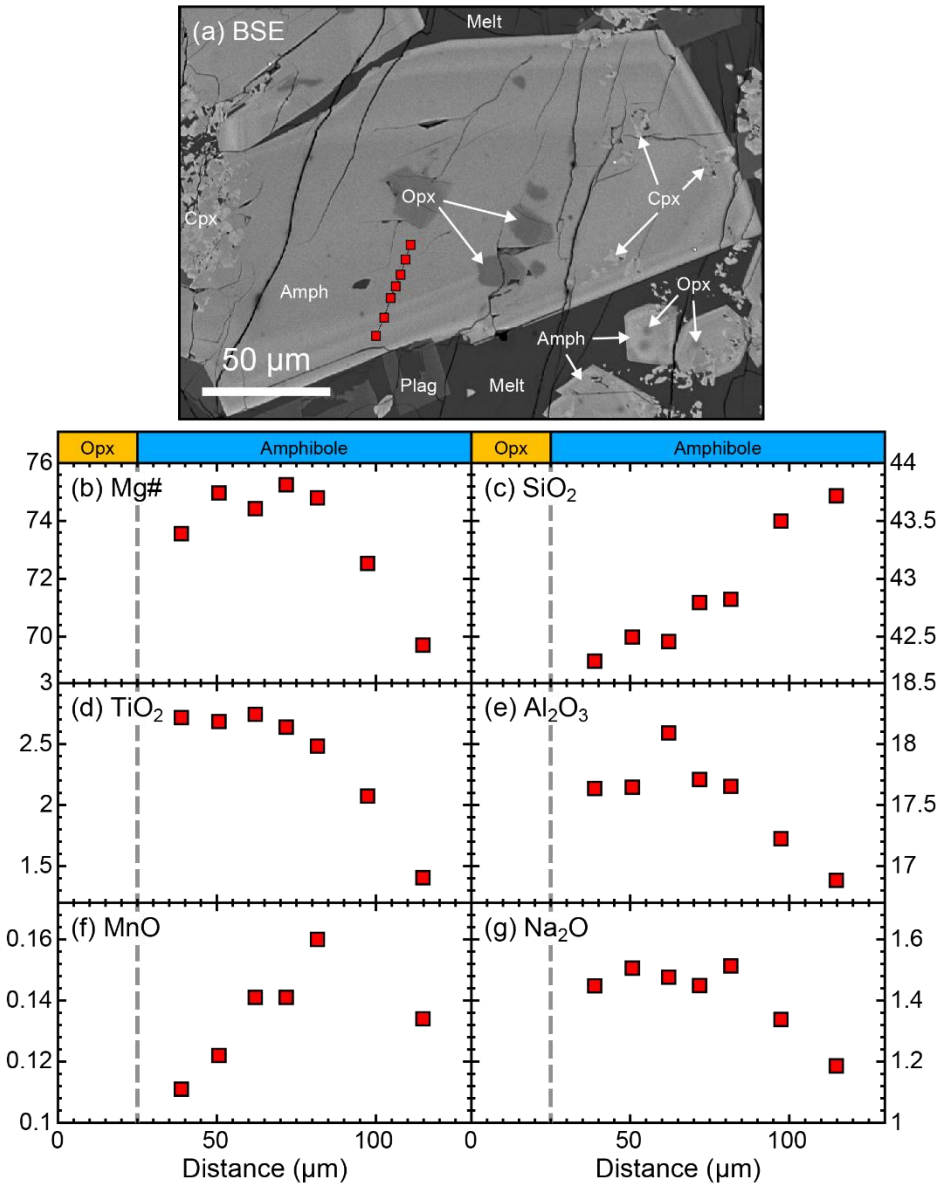

Figure S3. BSE image and electron microprobe data showing the chemical zoning of an amphibole grain. (a) Core-to-rim zoned amphibole in peridotite from MBH12. (b-g) Variations of Mg# and oxide abundances (in wt%) in amphibole as a function of distance from the amphibole core. Red squares in (a) mark positions of the probe analyses plotted in (b-g). Vertical dashed red lines in (b-g) mark the position of orthopyroxene-amphibole boundary. Note inclusions of orthopyroxenes in amphiboles.

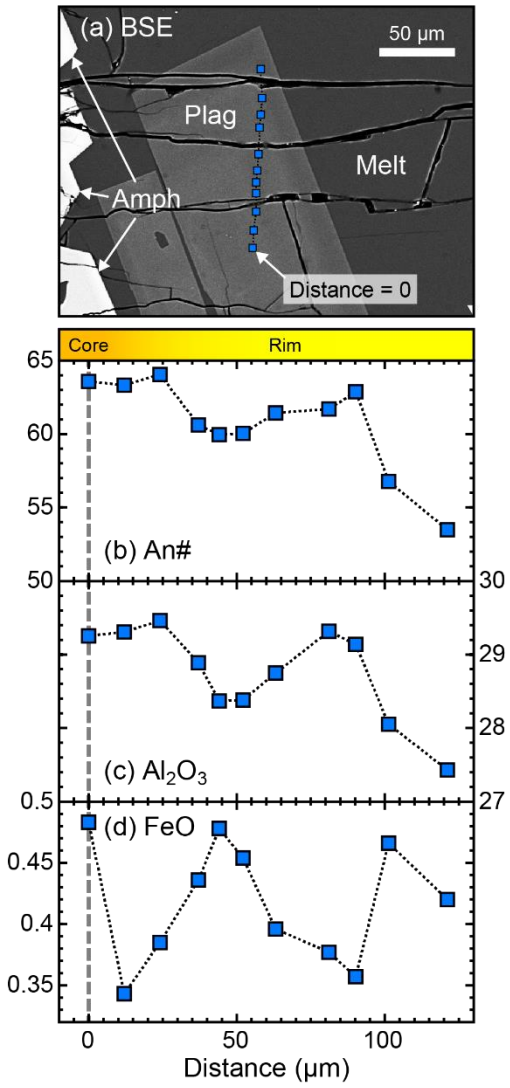

Figure S4. BSE image and electron microprobe data showing the chemical zoning of plagioclase grain. (a) Core-to-rim zoned plagioclase in amphibole gabbronorite from BAH13. (b-d) Variations of An# and oxide abundances (in wt%) in plagioclase as a function of distance from the plagioclase core. Blue squares in (a) mark positions of the probe analyses plotted in (b-d).

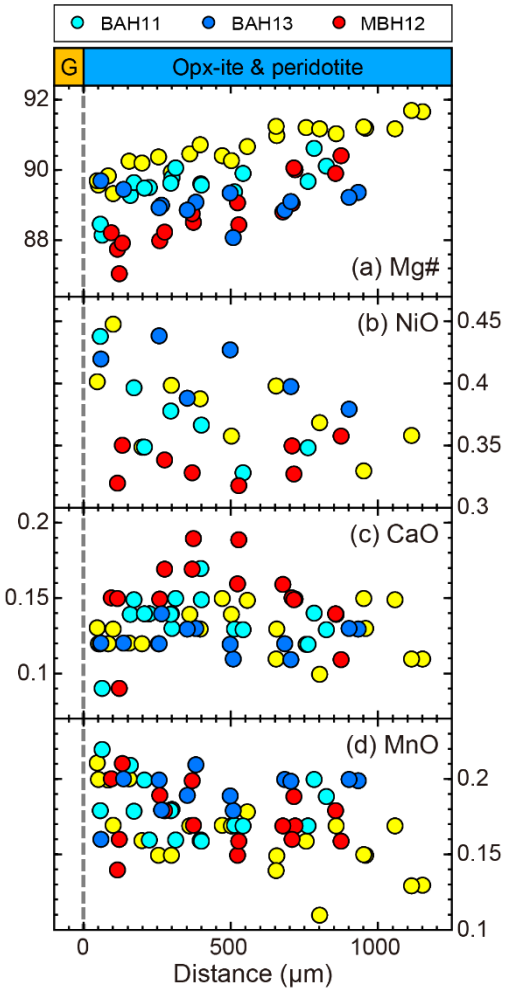

Figure S5. Plots of Mg# and oxide abundances (in wt%) in olivine as a function of distance from the gabbronorite-orthopyroxenite interface (dashed lines). Cyan, blue, red, and yellow circles are data from BAH11, BAH13, BAH12, and BAH8 (Wang et al. 2016), respectively.

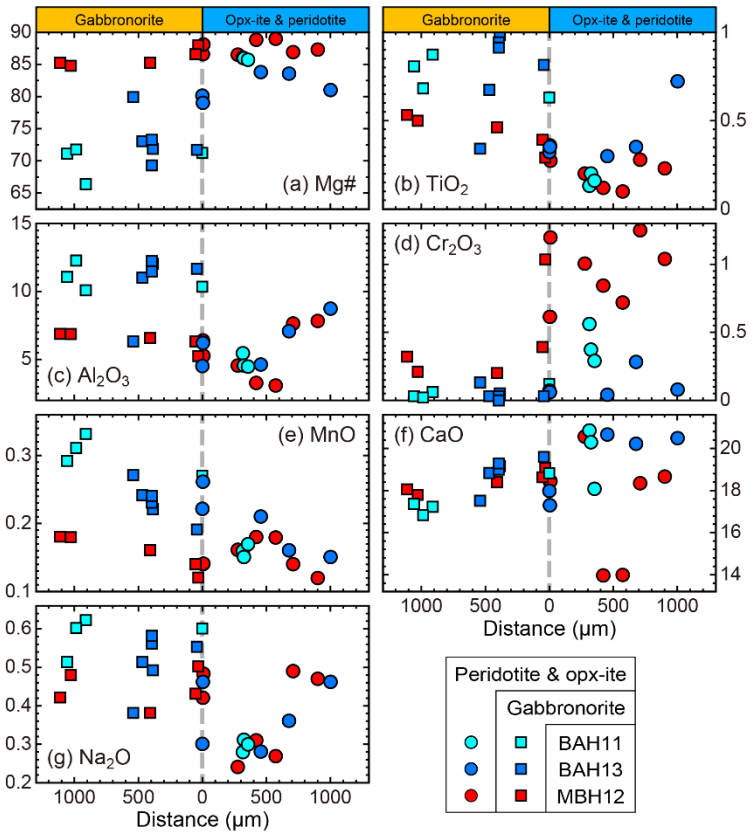

Figure S6. Plots of Mg# and oxide abundances (in wt%) in clinopyroxene as a function of distance from the gabbronorite-orthopyroxenite interface (dashed lines). Circles represent clinopyroxene in the orthopyroxenite and peridotite regions, and squares represent those in the gabbronorite regions.

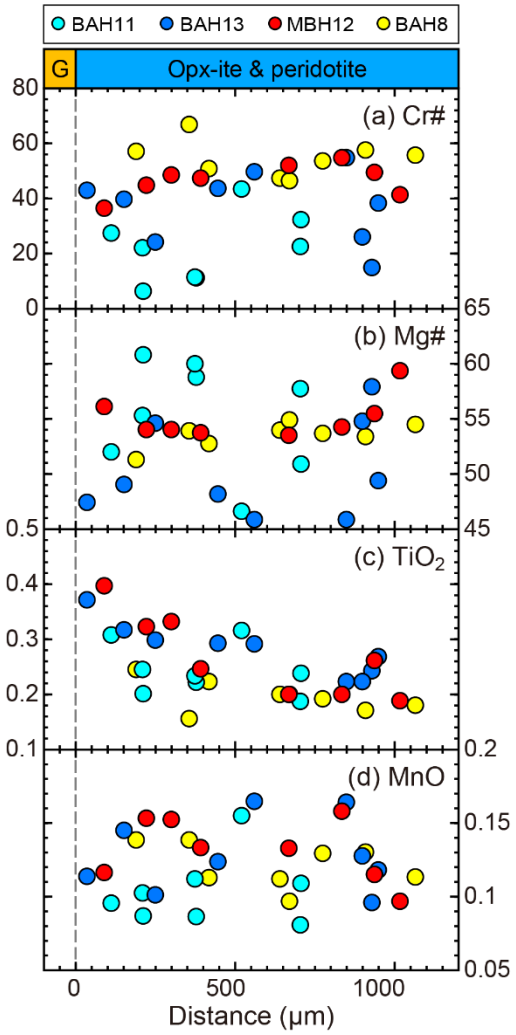

Figure S7. Plots of Cr#, Mg#, and oxide abundances (in wt%) in spinel as a function of distance from the gabbronorite-orthopyroxenite interface (dashed lines).

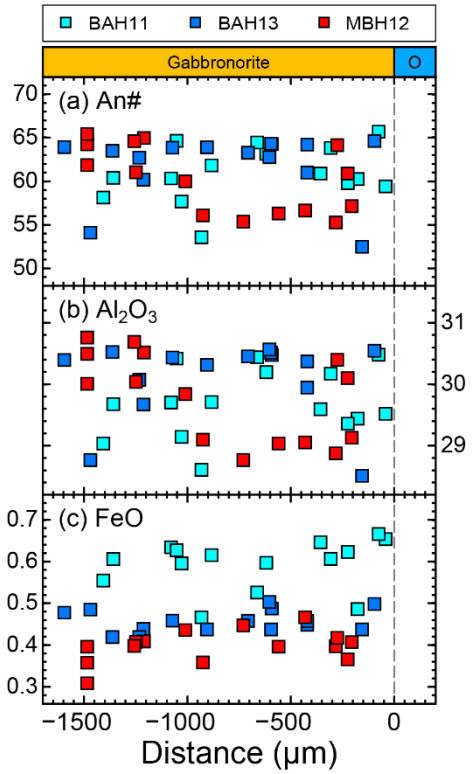

Figure S8. Plots of An# and oxide abundances (in wt%) in plagioclase as a function of distance from the gabbronorite-orthopyroxenite interface (dashed lines).

Table S1-1. Electron microprobe data of amphibole in BAH11

SiO_2	TiO_2	Al_2O_3	Cr_2O_3	FeO	MnO	MgO	CaO	Na_2O	Total	Mg#	X
42.11	1.93	13.14	0.05	16.68	0.37	10.79	10.55	1.74	97.36	53.56	4
42.00	2.36	13.61	0.00	17.05	0.39	10.71	9.93	1.78	97.83	52.82	-40
39.97	3.74	14.37	0.02	18.28	0.39	9.70	9.34	2.16	97.96	48.61	-5
41.67	1.47	16.78	0.05	7.21	0.10	17.10	10.46	2.79	97.63	80.87	127
42.75	0.83	15.87	0.04	6.96	0.08	17.65	10.90	2.66	97.73	81.89	197
44.10	0.47	15.31	0.04	7.15	0.12	18.04	10.68	2.38	98.27	81.81	298
42.48	1.19	15.63	0.14	6.80	0.10	17.51	10.82	2.67	97.34	82.11	402
44.49	0.37	14.28	0.31	6.63	0.14	18.53	10.76	2.30	97.79	83.28	843
40.14	3.38	14.01	0.00	18.23	0.40	9.27	9.80	1.93	97.17	47.55	-300
40.35	3.31	14.04	0.00	18.33	0.43	9.37	9.55	2.03	97.40	47.68	-924
39.83	3.14	15.02	0.01	18.47	0.41	8.97	9.33	1.83	97.02	46.40	-1007

Table S1-2. Electron microprobe data of olivine in BAH11

SiO_2	TiO_2	Al_2O_3	Cr_2O_3	FeO	MnO	MgO	CaO	Na_2O	NiO	Total	Mg#	X
40.34	0.02	0.05	0.05	11.41	0.22	47.60	0.09	ND	NA	99.76	88.15	62
40.56	0.01	0.04	0.06	10.43	0.21	48.71	0.14	ND	NA	100.18	89.28	160
40.68	0.01	0.06	0.04	10.19	0.16	48.71	0.14	ND	NA	99.99	89.50	223
40.46	0.01	0.03	0.05	9.93	0.18	48.89	0.13	0.01	NA	99.69	89.77	300
40.66	ND	0.13	0.06	9.63	0.16	48.96	0.15	0.04	NA	99.79	90.06	313
40.53	ND	0.08	0.05	10.08	0.16	48.76	0.17	ND	NA	99.83	89.61	397
40.43	0.01	0.04	0.06	10.33	0.17	48.81	0.13	0.02	NA	100.00	89.39	512
40.65	ND	0.04	0.05	9.15	0.20	49.58	0.14	ND	NA	99.82	90.62	782
40.86	0.01	0.03	0.05	9.68	0.19	49.50	0.13	ND	NA	100.44	90.11	825
40.65	ND	0.06	0.03	11.12	0.18	47.84	0.12	ND	0.44	100.45	88.46	58
40.89	0.01	0.03	0.07	10.09	0.18	48.99	0.15	ND	0.40	100.81	89.64	172
40.76	0.01	0.03	0.05	10.19	0.20	48.61	0.14	0.01	0.35	100.35	89.48	206
40.74	ND	0.05	0.03	10.11	0.18	48.98	0.14	ND	0.38	100.62	89.62	297
40.92	0.01	0.02	0.07	10.17	0.16	49.05	0.15	ND	0.37	100.91	89.58	400
40.88	0.01	0.06	0.08	9.85	0.17	49.17	0.13	0.01	0.33	100.68	89.90	542
40.78	0.01	0.03	0.05	10.06	0.17	48.98	0.12	ND	0.35	100.55	89.67	763

Table S1-3. Electron microprobe data of orthopyroxene in BAH11

SiO_2	TiO_2	Al_2O_3	Cr_2O_3	FeO	MnO	MgO	CaO	Na_2O	Total	Mg#	X
48.53	0.20	10.72	0.06	14.66	0.33	24.37	1.35	0.05	100.28	74.77	29
50.94	0.13	7.34	1.00	11.14	0.29	27.79	1.42	0.05	100.10	81.64	42
52.46	0.10	6.78	0.78	7.90	0.19	31.03	1.17	0.03	100.45	87.50	60
52.16	0.09	7.11	0.84	7.89	0.19	30.84	1.24	0.05	100.41	87.45	83
54.93	0.06	3.43	0.36	7.17	0.18	32.30	1.63	0.04	100.11	88.93	103
52.69	0.14	3.57	0.04	14.63	0.40	26.52	1.50	0.04	99.54	76.37	1
52.56	0.14	4.78	0.10	13.33	0.35	26.99	1.94	0.09	100.27	78.30	21
53.59	0.08	4.08	0.58	10.54	0.29	29.45	1.41	0.05	100.07	83.28	40
52.77	0.10	6.38	0.72	7.59	0.18	31.09	1.39	0.04	100.27	87.95	94
54.96	0.05	3.46	0.28	7.25	0.18	32.23	1.82	0.06	100.30	88.79	99
55.44	0.05	2.70	0.57	6.49	0.18	32.98	1.65	0.05	100.10	90.06	485
54.38	0.09	4.28	0.09	7.73	0.18	32.09	1.39	0.03	100.24	88.10	472
51.80	0.07	6.50	0.25	8.52	0.24	31.36	1.11	0.01	99.86	86.77	470
51.82	0.12	7.44	0.23	8.23	0.19	30.46	1.75	0.04	100.27	86.84	781
48.05	0.35	10.30	0.05	15.96	0.35	23.40	1.47	0.10	100.02	72.33	-202
48.44	0.38	7.63	0.05	18.43	0.48	21.85	2.11	0.04	99.41	67.88	-264
46.78	0.35	12.00	0.02	17.18	0.42	22.05	1.56	0.10	100.46	69.58	-875
49.05	0.26	9.05	0.06	14.74	0.38	24.20	1.99	0.09	99.80	74.53	-1003

Table S1-4. Electron microprobe data of clinopyroxene in BAH11

SiO_2	TiO_2	Al_2O_3	Cr_2O_3	FeO	MnO	MgO	CaO	Na_2O	Total	Mg#	X
46.82	0.63	10.34	0.12	9.33	0.27	12.96	18.80	0.60	99.86	71.23	18
50.63	0.13	5.45	0.56	4.91	0.16	16.97	20.85	0.28	99.94	86.04	335
51.18	0.20	4.53	0.37	5.11	0.15	17.51	20.20	0.31	99.55	85.93	346
51.81	0.16	4.47	0.29	5.64	0.17	19.05	18.06	0.30	99.95	85.76	375
46.31	0.68	12.23	0.02	9.39	0.31	13.39	16.78	0.60	99.69	71.77	-966
46.38	0.87	10.04	0.06	11.44	0.33	12.67	17.15	0.62	99.55	66.38	-891
46.35	0.80	10.99	0.03	9.67	0.29	13.36	17.23	0.51	99.24	71.12	-1037

Table S1-5. Electron microprobe data of spinel in BAH11

SiO_2	TiO_2	Al_2O_3	Cr_2O_3	FeO	MnO	MgO	CaO	Total	Mg#	Cr#	X
0.13	12.35	5.12	0.07	76.17	0.27	1.38	0.07	95.56	3.14	0.91	-789
0.11	10.52	6.01	0.02	76.00	0.25	1.45	0.05	94.40	3.28	0.22	-1324
0.12	9.75	7.32	0.05	75.93	0.23	1.60	0.07	95.07	3.62	0.46	-577
0.11	10.37	6.65	0.03	76.32	0.23	1.58	0.05	95.34	3.56	0.30	-367
0.11	11.64	5.26	0.07	77.34	0.27	1.37	0.07	96.14	3.07	0.89	-322
0.13	9.22	8.02	0.02	75.98	0.22	1.66	0.06	95.30	3.75	0.17	-75
0.17	10.25	6.00	0.03	75.96	0.22	1.49	0.10	94.22	3.37	0.34	-6
0.12	0.31	36.70	20.55	25.87	0.10	15.73	0.11	99.49	52.01	27.31	112
0.12	0.24	39.77	16.75	24.06	0.10	16.72	0.15	97.91	55.33	22.03	210
0.17	0.20	52.92	5.28	21.01	0.09	18.30	0.10	98.06	60.82	6.28	212
0.24	0.22	49.16	9.34	22.00	0.09	17.60	0.14	98.78	58.78	11.30	377
0.13	0.23	47.68	9.19	22.21	0.11	18.68	0.07	98.30	59.98	11.45	373
0.13	0.31	26.32	30.04	26.84	0.15	13.15	0.05	96.98	46.61	43.37	520
0.13	0.23	33.12	23.52	24.75	0.11	14.40	0.13	96.39	50.92	32.27	706
0.11	0.19	41.03	17.75	22.56	0.08	17.30	0.11	99.12	57.74	22.49	704

Table S1-6. Electron microprobe data of plagioclase in BAH11

SiO_2	TiO_2	Al_2O_3	FeO	MgO	CaO	Na_2O	K_2O	Total	An	X
53.99	0.04	29.66	0.49	0.11	12.02	4.29	0.14	100.75	60.76	-177
53.94	0.02	29.69	0.63	0.09	12.19	4.43	0.15	101.13	60.33	-224
53.81	0.03	29.80	0.66	0.11	11.97	4.42	0.15	100.95	59.95	-41
52.30	0.04	30.67	0.67	0.08	13.06	3.69	0.12	100.62	66.17	-75
52.93	0.01	30.35	0.61	0.09	12.60	3.86	0.13	100.59	64.34	-307
53.63	0.03	29.77	0.65	0.05	12.12	4.21	0.14	100.60	61.40	-357
52.82	0.01	30.36	0.60	0.07	12.58	3.97	0.13	100.54	63.65	-619
52.63	0.05	30.69	0.53	0.06	12.90	3.86	0.11	100.82	64.87	-663
53.70	0.01	29.92	0.62	0.09	12.16	4.05	0.15	100.71	62.40	-883
55.48	0.02	28.82	0.47	0.02	10.73	5.01	0.20	100.74	54.20	-932
54.17	0.05	29.38	0.60	0.09	11.71	4.65	0.15	100.81	58.19	-1029
53.72	0.04	29.99	0.64	0.04	12.08	4.29	0.15	100.96	60.88	-1079
52.37	0.01	30.56	0.63	0.05	12.90	3.82	0.12	100.47	65.11	-1052
54.29	0.02	29.32	0.56	0.15	11.86	4.62	0.15	100.98	58.65	-1407
53.54	0.03	29.88	0.61	0.08	12.11	4.29	0.15	100.69	60.94	-1359

Table S1-7. Electron microprobe data of melt in BAH11

SiO_2	TiO_2	Al_2O_3	Cr_2O_3	FeO	MnO	MgO	CaO	Na_2O	K_2O	Total	Mg#	X
65.24	0.32	15.56	0.07	3.46	0.12	0.79	4.31	1.97	1.18	93.03	28.93	-36
64.64	0.39	15.77	0.05	3.50	0.16	0.80	4.53	2.28	1.29	93.49	28.95	-236
64.87	0.37	15.71	0.13	3.61	0.18	0.81	4.43	2.45	1.37	93.98	28.57	-397
64.99	0.36	15.63	0.05	3.52	0.12	0.80	4.35	2.39	1.31	93.51	28.83	-645
64.62	0.44	15.54	0.03	3.38	0.13	0.81	4.50	1.99	1.29	92.76	29.93	-693
63.81	0.56	16.09	0.00	3.48	0.12	0.80	4.60	2.22	1.28	92.95	29.07	-651
63.78	0.43	16.19	0.10	3.38	0.19	0.83	4.66	2.45	1.32	93.40	30.45	-389
64.22	0.44	15.70	0.04	3.47	0.14	0.81	4.56	2.42	1.31	93.11	29.38	-622
64.89	0.38	15.68	0.02	3.22	0.15	0.84	4.51	2.53	1.24	93.48	31.74	-82
63.93	0.49	15.85	0.25	3.46	0.17	0.80	4.61	2.39	1.30	93.24	29.19	-494
64.94	0.39	15.48	0.19	3.60	0.15	0.76	4.43	2.45	1.30	93.75	27.34	-956
64.59	0.45	15.72	0.00	3.61	0.14	0.78	4.47	2.09	1.28	93.17	27.81	-1057
64.89	0.34	15.72	0.00	3.53	0.15	0.82	4.36	3.08	1.37	94.25	29.28	-1032

Table S2-1. Electron microprobe data of amphibole in BAH13

SiO_2	TiO_2	Al_2O_3	Cr_2O_3	FeO	MnO	MgO	CaO	Na_2O	Total	Mg#	X
41.30	2.42	14.63	0.02	13.59	0.22	12.79	10.54	2.21	97.71	62.65	-395
40.73	2.34	15.23	0.01	13.79	0.23	12.65	10.27	2.34	97.58	62.05	-380
40.28	2.38	15.79	0.00	14.05	0.21	12.22	10.17	2.26	97.36	60.79	-385
39.10	2.30	17.89	0.01	13.63	0.21	11.76	10.26	2.25	97.42	60.60	-36
39.68	2.10	17.31	0.01	13.55	0.22	12.12	10.33	2.43	97.76	61.46	-127
41.53	1.80	16.41	0.02	7.95	0.14	16.36	10.59	2.46	97.26	78.58	194
43.10	0.54	15.75	0.12	7.25	0.16	17.35	10.88	2.24	97.40	81.01	436
44.33	0.54	13.94	0.26	7.28	0.15	18.16	10.47	2.05	97.18	81.64	701
42.40	1.59	16.12	0.05	7.75	0.14	17.04	10.13	2.52	97.75	79.67	956

Table S2-2. Electron microprobe data of olivine in BAH13

SiO_2	TiO_2	Al_2O_3	Cr_2O_3	FeO	MnO	MgO	CaO	Na_2O	NiO	Total	Mg#	X
40.60	0.00	0.01	0.06	10.18	0.20	48.42	0.12	ND	NA	99.60	89.45	136
40.69	0.02	0.02	0.06	10.32	0.20	48.67	0.13	ND	NA	100.09	89.37	933
40.53	0.01	0.02	0.06	10.76	0.20	48.11	0.12	0.02	NA	99.84	88.85	684
40.49	ND	0.02	0.04	11.52	0.18	47.75	0.11	0.04	NA	100.15	88.08	508
40.59	0.01	0.03	0.05	10.55	0.21	48.33	0.13	0.01	NA	99.91	89.09	383
40.60	ND	0.02	0.05	10.65	0.18	48.31	0.14	ND	NA	99.94	88.99	266
40.58	0.01	0.01	0.05	10.43	0.20	48.45	0.13	ND	0.38	100.24	89.22	902
40.76	ND	ND	0.06	10.60	0.20	48.58	0.11	ND	0.40	100.72	89.09	705
40.67	ND	ND	0.06	10.38	0.19	48.85	0.12	ND	0.43	100.70	89.35	499
40.71	ND	0.02	0.07	10.78	0.19	48.23	0.13	ND	0.39	100.52	88.86	352
40.60	0.01	0.03	0.05	10.69	0.20	48.20	0.12	ND	0.44	100.35	88.93	258
40.74	ND	0.01	0.07	9.96	0.16	48.60	0.12	0.01	0.42	100.07	89.69	59

Table S2-3. Electron microprobe data of orthopyroxene in BAH13

SiO_2	TiO_2	Al_2O_3	Cr_2O_3	FeO	MnO	MgO	CaO	Na_2O	Total	Mg#	X	Comment
51.77	0.15	7.31	0.34	10.11	0.26	28.68	1.67	0.03	100.30	83.49	-330	Core
51.30	0.18	7.81	0.26	10.21	0.27	28.43	1.77	0.04	100.26	83.23	-295	Core
51.81	0.16	7.04	0.23	10.35	0.28	28.74	1.62	0.08	100.32	83.19	-380	Core
51.85	0.16	6.78	0.20	10.24	0.26	28.95	1.63	0.05	100.12	83.44	-325	Core
55.51	0.06	3.12	0.44	7.08	0.20	32.81	1.16	ND	100.37	89.20	126	Core
55.49	0.06	3.03	0.43	7.01	0.19	32.80	1.16	0.02	100.21	89.29	145	Core
55.48	0.06	3.18	0.43	6.92	0.18	32.82	1.15	0.02	100.25	89.42	125	Core
52.39	0.13	6.19	0.87	9.07	0.25	29.79	1.41	0.07	100.17	85.41	40	Rim
54.91	0.08	3.08	0.52	8.51	0.22	31.44	1.39	0.07	100.22	86.82	29	Rim
54.51	0.10	3.56	0.26	8.94	0.26	30.50	1.64	0.06	99.84	85.88	8	Rim
53.47	0.07	5.65	0.79	7.10	0.16	31.82	1.36	0.05	100.48	88.88	913	Core
52.40	0.11	7.11	0.52	8.11	0.17	30.87	1.31	0.01	100.60	87.15	911	Rim
52.69	0.07	6.48	0.97	7.17	0.17	31.31	1.19	0.04	100.07	88.62	580	Core
52.00	0.16	7.49	0.19	8.51	0.20	30.21	1.49	0.05	100.31	86.35	623	Rim
52.41	0.12	6.77	0.50	7.76	0.20	30.83	1.29	0.03	99.93	87.63	624	Rim
53.30	0.09	5.47	0.79	7.19	0.20	31.66	1.18	0.02	99.90	88.70	624	Core

Table S2-4. Electron microprobe data of clinopyroxene in BAH13

SiO_2	TiO_2	Al_2O_3	Cr_2O_3	FeO	MnO	MgO	CaO	Na_2O	Total	Mg#	X
50.22	0.34	6.30	0.13	7.58	0.27	16.93	17.44	0.38	99.59	79.93	-541
45.51	0.98	11.98	0.05	8.73	0.22	12.51	19.07	0.49	99.54	71.87	-387
46.33	0.67	10.94	0.03	8.67	0.24	13.19	18.70	0.51	99.28	73.06	-470
46.15	0.94	11.44	0.03	8.44	0.23	12.98	18.94	0.56	99.71	73.27	-395
45.27	0.91	12.21	ND	9.39	0.24	11.88	19.23	0.58	99.71	69.28	-395
51.31	0.32	4.51	0.07	7.62	0.22	17.23	17.88	0.30	99.45	80.12	-48
50.21	0.35	6.18	0.06	7.92	0.26	16.74	17.19	0.46	99.38	79.03	-12
45.66	0.81	11.60	0.03	8.70	0.19	12.38	19.47	0.55	99.39	71.72	-43
51.16	0.30	4.61	0.04	5.77	0.21	16.77	20.62	0.28	99.77	83.82	456
49.43	0.35	7.06	0.28	5.66	0.16	16.11	20.12	0.36	99.53	83.54	676
47.86	0.72	8.69	0.08	6.21	0.15	14.86	20.38	0.46	99.42	81.01	1001

Table S2-5. Electron microprobe data of spinel in BAH13

SiO_2	TiO_2	Al_2O_3	Cr_2O_3	FeO	MnO	MgO	CaO	Total	Mg#	Cr#	X
0.20	0.36	26.85	30.22	26.05	0.11	13.20	0.03	96.28	47.45	43.02	36
0.14	0.31	28.57	28.03	25.55	0.14	13.81	0.08	95.88	49.06	39.70	151
0.12	0.29	39.15	18.65	24.15	0.10	16.32	0.08	97.93	54.64	24.22	250
0.13	0.28	26.70	30.88	25.65	0.12	13.38	0.17	96.58	48.19	43.68	446
0.10	0.28	23.39	34.41	26.36	0.16	12.52	0.15	96.72	45.84	49.67	561
0.09	0.22	21.14	37.97	25.76	0.16	12.25	0.09	97.04	45.87	54.65	848
0.97	0.24	46.74	12.18	22.41	0.10	17.29	0.16	99.06	57.89	14.89	928
0.35	0.26	29.74	27.51	25.76	0.12	14.10	0.09	97.15	49.38	38.29	950
0.12	0.22	38.47	20.06	23.23	0.13	15.78	0.11	97.22	54.77	25.92	900

Table S2-6. Electron microprobe data of plagioclase in BAH13

SiO_2	TiO_2	Al_2O_3	FeO	MgO	CaO	Na_2O	K_2O	Total	An	X
52.23	0.01	30.67	0.50	0.06	12.97	3.84	0.13	100.41	65.11	-96
55.42	0.01	28.68	0.44	0.03	10.65	5.23	0.15	100.60	52.95	-156
52.79	0.02	30.49	0.45	0.06	12.65	3.81	0.13	100.39	64.72	-421
53.19	0.04	30.11	0.46	0.04	12.31	4.27	0.12	100.55	61.44	-421
52.62	0.03	30.64	0.49	0.08	12.73	3.84	0.11	100.54	64.69	-593
52.12	0.04	30.69	0.44	0.07	13.15	3.96	0.11	100.58	64.73	-596
52.35	0.02	30.97	0.51	0.05	13.09	4.22	0.11	101.32	63.16	-604
53.52	0.02	29.74	0.44	0.08	12.00	4.31	0.12	100.24	60.61	-1213
52.19	0.02	30.58	0.42	0.03	12.83	4.01	0.10	100.18	63.87	-1364
54.94	0.04	29.07	0.49	0.03	11.19	5.14	0.16	101.06	54.61	-1470
52.66	0.01	30.54	0.48	0.08	12.71	3.89	0.11	100.48	64.36	-1596
53.02	0.04	30.14	0.42	0.08	12.41	3.99	0.13	100.22	63.22	-1233
52.66	0.03	30.54	0.46	0.07	12.60	3.87	0.11	100.34	64.28	-1073
52.65	0.04	30.49	0.44	0.05	12.85	3.94	0.11	100.58	64.32	-906
52.30	0.02	30.60	0.46	0.08	12.87	4.05	0.12	100.49	63.72	-708

Table S2-7. Electron microprobe data of melt in BAH13

SiO_2	TiO_2	Al_2O_3	Cr_2O_3	FeO	MnO	MgO	CaO	Na_2O	K_2O	Total	Mg#	X
63.07	0.35	16.59	0.00	2.70	0.13	1.02	4.57	2.18	1.17	91.83	40.24	-142
63.05	0.16	16.97	0.00	2.72	0.13	1.10	4.60	2.88	1.24	92.90	41.89	-82
62.15	0.40	16.88	0.00	3.17	0.10	1.06	4.81	2.53	1.18	92.28	37.35	-639
62.12	0.42	16.78	0.03	3.26	0.12	1.01	4.76	2.37	1.17	92.06	35.58	-805
61.24	0.46	17.06	0.00	3.43	0.13	1.04	4.95	2.55	1.21	92.07	35.09	-1118
61.67	0.44	17.34	0.00	3.35	0.12	1.04	5.01	2.75	1.21	92.94	35.62	-938
61.81	0.52	16.95	0.00	3.51	0.11	1.04	4.91	2.82	1.18	92.86	34.56	-935
61.22	0.55	17.13	0.00	3.38	0.14	1.03	4.90	2.39	1.17	91.91	35.20	-1148
61.45	0.46	17.18	0.23	3.42	0.12	1.01	4.96	2.59	1.19	92.60	34.49	-1307
62.49	0.34	16.64	0.15	3.28	0.17	1.03	4.75	2.60	1.19	92.64	35.89	-1593
61.91	0.56	16.98	0.16	3.31	0.13	0.99	4.85	2.53	1.13	92.59	34.77	-1399
62.65	0.32	16.36	0.06	3.32	0.14	0.99	4.65	2.57	1.18	92.24	34.71	-1566

Table S2-8. Electron microprobe data of traverse on an orthopyroxene grain in BAH13 used in Figure S3

SiO_2	TiO_2	Al_2O_3	Cr_2O_3	FeO	MnO	MgO	CaO	Na_2O	K_2O	NiO	Total	D
53.19	0.10	5.92	0.66	6.30	0.09	31.05	1.08	0.03	0.02	0.14	98.57	0
53.12	0.05	6.06	0.78	6.61	0.24	31.02	1.19	0.03	0.02	0.12	99.24	16
52.72	0.05	5.97	0.80	6.92	0.18	31.35	1.11	0.02	0.00	0.06	99.18	35
53.11	0.11	6.06	0.74	6.50	0.11	30.92	1.02	0.01	0.03	0.13	98.73	42
51.94	0.10	7.29	0.44	7.58	0.12	29.70	1.29	0.05	0.01	0.10	98.62	50
50.66	0.10	8.77	0.34	8.38	0.13	28.98	1.61	0.00	0.00	0.14	99.10	65
50.97	0.17	7.82	0.03	8.46	0.18	29.65	1.45	0.02	0.00	0.11	98.85	80
51.36	0.26	7.59	0.05	8.48	0.13	29.96	1.04	0.00	0.01	0.15	99.03	90
50.73	0.28	8.70	0.00	9.64	0.32	28.81	0.92	0.02	0.00	0.10	99.52	100

Table S2-9. Electron microprobe data of traverse on a plagioclase grain in BAH13 used in Figure S5

SiO_2	TiO_2	Al_2O_3	Cr_2O_3	FeO	MnO	MgO	CaO	Na_2O	K_2O	Total	An	D
52.93	0.00	29.26	0.01	0.48	0.00	0.06	13.01	4.12	0.15	100.01	63.58	0
52.91	0.13	29.13	0.00	0.34	0.00	0.05	12.66	4.05	0.13	99.39	63.33	12
52.37	0.13	29.26	0.05	0.38	0.06	0.04	12.91	4.00	0.13	99.31	64.06	24
51.01	0.05	27.41	0.04	0.41	0.03	0.06	11.58	4.16	0.12	94.88	60.62	37
54.17	0.00	28.35	0.00	0.48	0.02	0.07	12.19	4.50	0.14	99.92	59.97	44
54.22	0.00	28.52	0.00	0.46	0.01	0.05	12.53	4.61	0.11	100.50	60.05	52
53.80	0.00	28.72	0.00	0.40	0.00	0.05	12.46	4.32	0.15	99.90	61.44	63
53.02	0.08	29.32	0.00	0.38	0.01	0.05	12.68	4.35	0.14	100.01	61.71	81
53.80	0.00	29.30	0.04	0.36	0.01	0.05	12.74	4.15	0.11	100.55	62.89	90
54.93	0.05	28.22	0.02	0.47	0.05	0.05	11.75	4.94	0.14	100.61	56.78	101
55.92	0.03	27.62	0.00	0.42	0.00	0.01	11.12	5.34	0.20	100.67	53.50	121

Table S3-1. Electron microprobe data of amphibole in MBH12

SiO_2	TiO_2	Al_2O_3	Cr_2O_3	FeO	MnO	MgO	CaO	Na_2O	Total	Mg#	X
41.11	1.82	17.54	0.14	10.34	0.18	13.70	10.76	2.66	98.24	70.25	-137
40.46	2.57	17.61	0.15	10.09	0.15	14.17	10.40	2.74	98.33	71.46	-111
41.79	0.78	18.01	0.09	9.29	0.18	14.92	10.37	2.41	97.85	74.11	92
40.88	2.98	17.26	0.04	7.41	0.11	16.46	10.01	2.85	98.00	79.84	114
41.39	1.81	16.78	0.13	10.44	0.18	13.87	10.76	2.47	97.83	70.31	-90
40.86	2.05	17.41	0.06	10.08	0.15	14.27	10.58	2.66	98.11	71.62	-79
41.42	1.61	17.55	0.01	9.28	0.17	14.71	10.49	2.48	97.71	73.86	96
42.37	2.15	16.41	0.02	7.04	0.12	17.33	9.55	2.96	97.95	81.44	260
41.67	2.53	16.72	0.03	6.88	0.14	17.17	9.89	2.83	97.84	81.65	391
42.72	2.55	15.84	0.03	6.70	0.15	17.65	9.74	2.75	98.12	82.44	560
43.18	0.86	16.44	0.40	6.15	0.10	18.12	10.21	2.78	98.25	84.01	981
39.59	2.75	18.11	0.04	10.42	0.18	13.60	10.55	2.65	97.88	69.94	-371
41.19	2.24	17.02	ND	10.21	0.17	14.26	10.40	2.69	98.17	71.34	-342
39.94	2.70	18.21	0.02	9.59	0.13	14.84	9.84	2.73	98.00	73.39	-1067
40.77	2.27	16.94	0.08	10.12	0.14	14.17	10.90	2.52	97.91	71.40	-1057
39.96	2.80	17.96	0.01	9.32	0.14	14.65	10.49	2.78	98.11	73.70	-1260
40.99	2.03	17.04	0.02	10.16	0.17	14.10	10.66	2.53	97.71	71.21	-1085

Table S3-2. Electron microprobe data of olivine in MBH12

SiO_2	TiO_2	Al_2O_3	Cr_2O_3	FeO	MnO	MgO	CaO	Na_2O	NiO	Total	Mg#	X
40.04	0.02	0.02	0.02	12.45	0.16	46.94	0.09	0.03	NA	99.77	87.05	122
40.24	0.01	0.03	0.03	11.35	0.20	47.67	0.15	ND	NA	99.68	88.22	95
40.34	0.01	0.03	0.08	11.61	0.19	47.71	0.15	ND	NA	100.13	87.99	259
40.42	ND	0.04	0.06	11.11	0.17	48.00	0.19	0.05	NA	100.04	88.51	374
40.46	0.01	0.02	0.07	10.62	0.15	48.50	0.16	0.01	NA	99.99	89.06	523
40.77	ND	0.02	0.06	9.76	0.17	49.31	0.15	0.01	NA	100.26	90.01	719
40.52	ND	0.04	0.06	10.87	0.17	48.40	0.16	ND	NA	100.22	88.81	677
40.65	0.01	0.01	0.06	9.85	0.18	49.21	0.14	0.03	NA	100.14	89.90	856
40.21	ND	0.01	0.04	11.82	0.14	47.50	0.15	0.02	0.32	100.22	87.75	116
40.35	0.02	ND	0.04	11.54	0.21	47.14	0.22	0.03	0.35	100.08	87.92	133
40.48	0.01	0.02	0.05	11.38	0.18	47.88	0.17	0.01	0.34	100.52	88.24	276
40.62	0.01	0.03	0.05	10.90	0.20	48.25	0.17	ND	0.33	100.55	88.75	370
40.67	ND	0.04	0.05	11.21	0.16	48.13	0.19	0.02	0.32	100.80	88.44	528
40.55	0.01	0.03	0.04	10.57	0.16	48.19	0.15	ND	0.35	100.06	89.04	709
40.96	0.01	0.03	0.07	9.73	0.19	49.41	0.15	0.01	0.33	100.89	90.05	715
40.93	0.01	0.02	0.05	9.40	0.16	49.68	0.11	ND	0.36	100.72	90.40	876

Table S3-3. Electron microprobe data of orthopyroxene in MBH12

SiO_2	TiO_2	Al_2O_3	Cr_2O_3	FeO	MnO	MgO	CaO	Na_2O	Total	Mg#	X	Comment
52.47	0.22	7.04	0.55	7.85	0.17	30.21	1.89	0.04	100.43	87.28	34	
54.48	0.12	4.96	0.40	6.39	0.15	32.62	0.96	0.10	100.18	90.10	2	
50.91	0.34	8.89	0.02	9.16	0.19	29.07	1.69	0.06	100.35	84.98	37	
52.53	0.20	6.61	0.49	7.93	0.14	30.49	1.69	0.04	100.12	87.27	28	
51.74	0.32	8.21	0.06	7.88	0.19	29.89	1.65	0.03	99.97	87.12	695	
51.83	0.29	8.29	0.12	7.98	0.16	30.23	1.30	0.06	100.27	87.10	665	
51.21	0.26	9.70	0.10	7.67	0.17	29.81	1.54	0.05	100.50	87.39	856	
52.17	0.22	7.41	0.15	8.55	0.23	30.10	1.49	0.03	100.34	86.26	856	
49.44	0.46	10.07	0.02	11.57	0.23	26.85	1.81	0.06	100.52	80.53	-1067	In center part of amph
49.79	0.33	9.83	0.04	10.94	0.21	27.48	1.22	0.04	99.89	81.74	-1305	In center part of amph

Table S3-4. Electron microprobe data of clinopyroxene in MBH12

SiO_2	TiO_2	Al_2O_3	Cr_2O_3	FeO	MnO	MgO	CaO	Na_2O	Total	Mg#	X
51.09	0.29	5.23	1.03	4.37	0.12	17.93	18.98	0.50	99.53	87.97	-44
50.56	0.36	6.39	0.61	4.94	0.14	17.89	18.36	0.42	99.66	86.59	-7
50.86	0.39	6.30	0.39	4.89	0.14	17.69	18.56	0.43	99.64	86.57	-66
51.05	0.27	5.23	1.19	4.40	0.14	18.27	18.34	0.48	99.37	88.10	-5
50.81	0.20	4.51	1.00	4.78	0.16	17.21	20.43	0.24	99.34	86.52	266
53.36	0.12	3.25	0.84	5.07	0.18	22.69	13.92	0.31	99.74	88.86	408
53.92	0.10	3.11	0.72	5.02	0.18	22.85	14.01	0.27	100.18	89.03	560
49.93	0.28	7.63	1.25	4.66	0.14	17.35	18.36	0.49	100.08	86.91	697
49.91	0.23	7.83	1.04	4.48	0.12	17.24	18.66	0.47	99.98	87.28	891
50.53	0.46	6.55	0.20	5.41	0.16	17.56	18.31	0.38	99.56	85.26	-421
50.47	0.50	6.87	0.21	5.70	0.18	17.82	17.80	0.48	100.03	84.79	-1041
50.29	0.53	6.85	0.32	5.43	0.18	17.60	17.98	0.42	99.57	85.25	-1124

Table S3-5. Electron microprobe data of spinel in MBH12

SiO_2	TiO_2	Al_2O_3	Cr_2O_3	FeO	MnO	MgO	CaO	Total	Mg#	Cr#	X
0.13	0.39	34.09	29.26	20.32	0.12	14.59	0.06	98.07	56.14	36.54	89
0.13	0.33	26.34	36.90	20.93	0.15	13.80	0.18	97.98	54.02	48.45	300
0.14	0.32	28.45	34.45	20.74	0.15	13.67	0.20	97.34	54.02	44.82	222
0.14	0.24	26.99	36.11	20.55	0.13	13.40	0.13	96.92	53.76	47.30	392
0.14	0.20	24.38	39.53	20.47	0.13	13.23	0.02	97.35	53.53	52.09	669
0.13	0.20	23.17	41.91	19.61	0.16	13.05	0.14	97.65	54.26	54.82	835
0.18	0.26	26.50	38.60	20.29	0.12	14.18	0.11	99.40	55.47	49.42	938
0.18	0.19	31.63	33.06	18.32	0.10	14.99	0.04	97.59	59.33	41.21	1017

Table S3-6. Electron microprobe data of plagioclase in MBH12

SiO_2	TiO_2	Al_2O_3	FeO	MgO	CaO	Na_2O	K_2O	Total	An	X
54.77	0.02	29.35	0.41	0.06	11.43	4.73	0.01	100.76	57.18	-206
53.53	0.01	30.46	0.37	0.03	12.38	4.39	0.01	101.19	60.91	-226
55.08	0.01	29.08	0.40	0.03	11.12	4.97	0.01	100.71	55.29	-283
54.85	0.01	29.34	0.40	0.06	11.46	4.91	0.01	101.04	56.33	-559
55.46	0.01	28.97	0.45	0.04	10.91	4.85	0.02	100.71	55.42	-730
54.74	0.02	29.24	0.36	0.02	11.24	4.86	0.01	100.49	56.10	-925
53.73	0.02	30.11	0.44	0.05	12.10	4.46	ND	100.91	59.99	-1011
52.51	0.02	30.62	0.41	0.07	12.87	3.83	0.01	100.34	65.00	-1211
53.13	0.04	30.22	0.41	0.07	12.36	4.35	0.02	100.60	61.09	-1250
52.18	0.01	30.82	0.40	0.04	13.03	3.94	0.01	100.43	64.63	-1258
52.88	0.04	30.66	0.36	0.09	12.63	3.88	0.01	100.55	64.27	-1485
52.30	0.03	30.93	0.31	0.09	13.06	3.81	0.01	100.55	65.45	-1485
53.52	0.03	30.30	0.40	0.04	12.44	4.24	ND	100.97	61.85	-1485
52.95	0.01	30.62	0.42	0.04	12.73	3.92	0.02	100.73	64.22	-276
54.63	0.02	29.26	0.47	0.05	11.45	4.84	0.01	100.71	56.66	-431

Table S3-7. Electron microprobe data of melt in MBH12

SiO_2	TiO_2	Al_2O_3	Cr_2O_3	FeO	MnO	MgO	CaO	Na_2O	K_2O	Total	Mg#	X
60.32	0.06	18.37	ND	2.21	0.05	1.76	5.60	0.58	0.05	89.00	58.67	41
58.94	0.08	18.10	0.25	2.39	0.09	1.73	5.72	2.32	0.05	89.67	56.34	136
61.99	0.21	16.52	0.03	2.07	0.06	1.32	5.31	2.29	0.05	89.84	53.20	-27
62.27	0.28	17.09	ND	2.12	0.06	1.32	5.57	2.52	0.06	91.34	52.60	-80
62.08	0.26	16.73	ND	2.37	0.10	1.28	5.70	2.33	0.06	90.91	49.05	-285
62.18	0.27	16.82	ND	2.35	0.07	1.31	5.72	2.67	0.06	91.45	49.84	-378
62.01	0.30	16.92	ND	2.45	0.11	1.30	5.70	2.48	0.05	91.32	48.61	-593
62.10	0.29	16.92	ND	2.51	0.10	1.27	5.71	2.79	0.05	91.77	47.42	-716
61.97	0.24	17.08	ND	2.48	0.10	1.31	5.76	2.45	0.06	91.46	48.50	-810
61.91	0.26	17.12	0.14	2.34	0.10	1.30	5.69	2.40	0.06	91.33	49.76	-1005
61.47	0.34	16.77	0.02	2.78	0.08	1.25	5.81	2.43	0.06	91.05	44.49	-1105
61.97	0.30	16.56	0.07	2.44	0.02	1.26	5.74	2.25	0.06	90.74	47.93	-1329
61.37	0.33	16.67	ND	2.62	0.09	1.22	5.81	2.42	0.04	90.57	45.36	-1358
60.98	0.35	17.27	ND	2.82	0.08	1.26	5.96	2.33	0.05	91.11	44.33	-1510

Table S3-8. Electron microprobe data of traverse on an amphibole grain with orthopyroxene in the center part in MBH12 used in Figure S4

SiO_2	TiO_2	Al_2O_3	Cr_2O_3	FeO	MnO	MgO	CaO	Na_2O	K_2O	NiO	Total	Mg#	D	Mineral
50.54	0.31	9.72	0.06	10.95	0.14	26.78	1.27	0.06	0.03	0.04	99.90	81.34	0.00	Opx
40.05	2.57	16.70	0.07	9.13	0.11	14.26	10.37	1.37	0.02	0.05	94.70	73.57	38.83	Amph
40.25	2.54	16.72	0.00	8.59	0.12	14.44	10.60	1.43	0.04	0.00	94.72	74.97	50.70	Amph
40.01	2.59	17.05	0.00	8.69	0.13	14.44	10.16	1.39	0.02	0.00	94.24	74.43	62.10	Amph
40.41	2.49	16.72	0.04	8.38	0.13	14.29	10.59	1.37	0.01	0.00	94.44	75.25	71.84	Amph
40.03	2.32	16.50	0.03	8.50	0.15	14.15	10.35	1.41	0.01	0.03	93.48	74.80	81.61	Amph
40.95	1.95	16.22	0.02	9.54	0.00	14.13	10.02	1.26	0.01	0.04	94.14	72.54	97.42	Amph
41.64	1.34	16.08	0.03	10.60	0.13	13.68	10.62	1.13	0.00	0.00	95.25	69.71	114.79	Amph